OCEANOGRAPHY

Biological export production controls upper ocean calcium carbonate dissolution and CO_2 buffer capacity

Eun Young Kwon[1,2]*, John P. Dunne[3], Kitack Lee[4]

Marine biogenic calcium carbonate ($CaCO_3$) cycles play a key role in ecosystems and in regulating the ocean's ability to absorb atmospheric carbon dioxide (CO_2). However, the drivers and magnitude of $CaCO_3$ cycling are not well understood, especially for the upper ocean. Here, we provide global-scale evidence that heterotrophic respiration in settling marine aggregates may produce localized undersaturated microenvironments in which $CaCO_3$ particles rapidly dissolve, producing excess alkalinity in the upper ocean. In the deep ocean, dissolution of $CaCO_3$ is primarily driven by conventional thermodynamics of $CaCO_3$ solubility with reduced fluxes of $CaCO_3$ burial to marine sediments beneath more corrosive North Pacific deep waters. Upper ocean dissolution, shown to be sensitive to ocean export production, can increase the neutralizing capacity for respired CO_2 by up to 6% in low-latitude thermocline waters. Without upper ocean dissolution, the ocean might lose 20% more CO_2 to the atmosphere through the low-latitude upwelling regions.

INTRODUCTION

Biogenic calcium carbonate minerals (mostly calcite and aragonite) are produced by organisms in the euphotic zone, the sunlit layer closest to the ocean surface. When the organisms die and sink through the water column, a portion of $CaCO_3$ minerals dissolves while the remaining portion is dissolved or buried in marine sediments. The magnitude of surface $CaCO_3$ export and subsequent dissolution in the water column—a process called the carbonate pump (*1*)—can influence the ocean's ability to absorb atmospheric CO_2 through a distribution of seawater alkalinity. Sinking biogenic $CaCO_3$ can also act as a ballast mineral for sinking organic particles (*2*, *3*), which in turn can control food supplies for marine organisms at depth and contribute to long-term carbon sequestration. Ocean acidification, caused by oceanic absorption of anthropogenic CO_2, has adverse effects on marine calcifiers by reducing calcification rates and decreasing seawater saturation state with respect to $CaCO_3$ minerals (*4*). However, the sensitivity of biogenic $CaCO_3$ cycling to seawater acidity is difficult to assess globally because of the diversity of calcifying organisms and their differing sensitivities to environmental conditions (*4*, *5*). Furthermore, our incomplete understanding of the drivers of $CaCO_3$ export and dissolution challenges a reliable projection of the future strength and efficiency of the carbonate pump and the oceanic carbon sink (*6*). The global ocean patterns of the carbonate pump's strength and efficiency and their environmental and biological controls can help constrain future sensitivities of the carbonate pump to climate and environmental changes.

The association between the spatial pattern of the carbonate pump and its environmental controls is yet to be underpinned by solid theoretical and observational lines of evidence. Satellite observations tend to point to higher calcification rates in high-latitude surface waters, whereas sediment trap data point to higher $CaCO_3$ export rates in waters at low latitudes (*7*, *8*), implying decoupling between the surface production and vertical export of biogenic $CaCO_3$ (*9*). The absence of global data on various types of calcifying organisms, ranging from those containing less soluble calcite (constituting coccolithophores and foraminifera) to those having more soluble aragonite or high-Mg calcite (constituting pteropods and fish bones), is another source of uncertainty with respect to the global ocean $CaCO_3$ cycle (*9*, *10*). A related uncertainty lies in where and how sinking $CaCO_3$ particles dissolve. While studies based on laboratory and in situ experiments focused on the abiotic effects of $CaCO_3$ solubility in acidified deep waters (*11*–*15*), studies based on sediment traps and alkalinity data highlighted that approximately 50% of $CaCO_3$ exported from the ocean surface is dissolved either in slightly oversaturated or close to saturated waters for calcite and aragonite minerals (*8*, *15*–*19*). These studies hypothesized that $CaCO_3$ particles are dissolved in organic matter aggregates or zooplankton guts where the release of CO_2 from the oxidation of organic matter and digestive acids generates highly acidic microenvironments. A tight association between metabolic respiration of sinking organic particles and $CaCO_3$ dissolution within the upper part of the twilight zone (upper 100 to 300 m) was confirmed in direct observations in the North Pacific (*15*, *18*) and in the North Atlantic (*20*); however, the relative importance of the abiotic versus biotic controls of the global ocean $CaCO_3$ dissolution rates and their effects on the seawater neutralizing capacity for atmospheric CO_2 have remained somewhat uncertain.

To estimate the global ocean cycling of biogenic $CaCO_3$, we use an ocean biogeochemistry model where $CaCO_3$ export and dissolution are empirically formulated in terms of the $CaCO_3$ mineral saturation states and organic carbon remineralization rates (see Materials and Methods). The model of $CaCO_3$ cycling is optimized against global observational datasets of alkalinity (*21*), dissolved inorganic carbon (DIC) (*21*), and the burial fluxes of inorganic carbon into marine sediments (see Materials and Methods) (*22*). The model also includes an observationally constrained ocean circulation field (*23*), satellite-based estimates of net primary production (NPP) (*24*, *25*), observed riverine inputs of nutrients and carbon (*26*, *27*), and the effects of water-column nitrification and denitrification (*28*) on alkalinity distribution (*29*). Hence, our model takes into account the lateral advection and mixing of alkalinity from coastal margins and alkalinity input from alkalinity-rich deep waters that are essential to accurately quantify $CaCO_3$ dissolution rates throughout the water

[1]Center for Climate Physics, Institute for Basic Science, Busan 46241, South Korea. [2]Pusan National University, Busan 46241, South Korea. [3]NOAA/OAR Geophysical Fluid Dynamics Laboratory, 201 Forrestal Rd, Princeton, NJ, USA. [4]Division of Environmental Science and Engineering, Pohang University of Science and Technology, Pohang, South Korea.
*Corresponding author. Email: ekwon957@gmail.com

column (*30*, *31*). We note that although some of the input data (e.g., NPP, riverine carbon inputs, and $CaCO_3$ burial fluxes into marine sediments) include coastal features, our coarse resolution model (2° × 2° horizontal resolution and 24 vertical layers) does not resolve the regional details of coastal ocean currents, shelf processes, and neritic $CaCO_3$ cycling. Hence, our global ocean estimates are inevitably limited to the $CaCO_3$ cycles in the open ocean.

An important aspect of this study is that we assess the model performance using the global observational compilations of sediment trap-based $CaCO_3$ flux data (*15*, *20*, *32*, *33*) and large-volume pump–based $CaCO_3$ concentration data (*34*–*36*), both measured within the ocean's upper twilight zone (upper 300 m). As shown below, the observed relationships between the vertical attenuations of $CaCO_3$ and particulate organic carbon (POC) fluxes or concentrations provide crucial constraints on the biogenic control of vertical $CaCO_3$ transfer efficiency above 300 m that is only weakly constrained by the observed tracer concentrations alone. This study builds upon a previous study of constraining the global ocean's organic carbon cycles (*37*) and includes both organic and inorganic carbon cycling from their surface export to sedimentary burial fluxes in a self-consistent manner. A more realistic representation of the upper ocean physical and biogeochemical processes, compared to previous global-scale assessments (*16*, *19*), helps elucidate the regional hotspots for the abiotic versus biotic drivers of $CaCO_3$ dissolution. Our numerical model framework also allows us to explore the global effects of $CaCO_3$ dissolution on the CO_2 buffer capacity of seawater. Below, we report the best estimates that are optimally consistent with the observational constraints (figs. S1 and S2). Uncertainties for our estimates are derived on the basis of a suite of model experiments, considering uncertainties in satellite-based NPP estimates and model formulations for $CaCO_3$ export and dissolution (see Materials and Methods).

RESULTS

Spatial patterns of $CaCO_3$ export and shallow (≤300 m) dissolution

Our model reveals large horizontal variability in the export ratio of $CaCO_3$ to POC at the base of the euphotic zone that is correlated with the degree of supersaturation at the sea surface (fig. S3). The $CaCO_3$ export ratio ranges from near-zero at high latitudes to 17% with an uncertainty range of 10 to 21% at low latitudes (averaged over 30°S to 30°N). When total organic carbon export (the sum of dissolved and POC) is considered, the range becomes slightly narrower from near-zero at high latitudes to 16% (with an uncertainty range of 9 to 19%) at low latitudes where dissolved organic carbon (DOC) is exported to the subsurface via the subduction of mode and intermediate waters. Although such spatial correspondence does not prove a causal relationship, saturation state–dependent calcification rates were commonly obtained in laboratory, culture, and mesocosm experiments (*4*, *5*). Higher $CaCO_3$ export ratios toward the low-latitude surface are also consistent with previous sediment trap- and model-based studies (*38*, *39*). Using the constrained $CaCO_3$ export ratio and the model estimate of POC export (*37*), we obtain the $CaCO_3$ export from the euphotic zone that ranges from near-zero in polar and oligotrophic regions to 20 g C m^{-2} $year^{-1}$ in highly productive regions (Fig. 1A) where POC export can reach as high as 150 g C m^{-2} $year^{-1}$ (fig. S3). When zonally averaged, the large spatial range is reduced to a meridional variation of 0 to 9 g C m^{-2} $year^{-1}$ for $CaCO_3$ and 11 to 94 g C m^{-2} $year^{-1}$ for POC export (Fig. 2A) due to substantial longitudinal heterogeneity.

The subsequent dissolution of $CaCO_3$ in the ocean's interior (water column and sediments combined) is highly variable in space (fig. S4). The most intensive dissolution occurs close to the base of the euphotic zone (roughly corresponding to the upper twilight zone shallower than 300 m) under areas where the surface is highly productive. When the vertical fluxes are normalized with respect to the export from the euphotic zone, the fraction at which the $CaCO_3$ exported from the base of the euphotic zone is dissolved (also termed dissolution efficiency hereinafter) within the upper 300 m exhibits a large horizontal variability of 0 to 70% in our optimal solution (Fig. 1B). A meridional variability of the zonally averaged dissolution fraction at 300 m ranges from 8 to 52% (Fig. 2A). When the uncertainty from the suite of model experiments is considered, the meridional variability extends to a range from 0 to 75%. To put it another way, the depth by which 70% of the surface exported $CaCO_3$ is dissolved varies from a depth of 240 to 3900 m in our best estimate and from a depth of 130 to 4300 m when the uncertainty is considered (Fig. 2C).

The most rapid vertical attenuation of $CaCO_3$ flux occurs in the mid-latitude North Atlantic and North Pacific around 40°N where the POC export is largest (Figs. 1B and 2A). Such rapid attenuation of sinking $CaCO_3$ fluxes was observed in the upper twilight zone of the North Pacific subpolar gyre (i.e., station 4 in fig. S5) (*15*), where our model indicates 53% (with an uncertainty of 0 to 76%) dissolution between 73 and 300 m at a grid cell located at 42°N, 158°W (Figs. 1B and 3B and fig. S5). Our model-based estimate agrees reasonably well with the observed value of 63 ± 3% dissolution (*15*) (Fig. 3 and fig. S5). The rapid attenuation of sinking $CaCO_3$ fluxes in the North Atlantic subpolar gyre is also qualitatively supported by sediment trap $CaCO_3$ fluxes reported to diminish by 84 ± 5% from 51 to 184 m at the Porcupine Abyssal Plain (PAP) station located at 49°N, 16°W (Fig. 3 and fig. S6) (*20*).

The dissolution hotspots within the upper twilight zone of the Northern Hemisphere mid-latitudes are followed in amplitude by large dissolution fractions within the upper twilight zone of the equatorial upwelling regions and the subantarctic zones where our model suggests that ~30% of the exported $CaCO_3$ dissolves within the upper 300 m (Figs. 1B and 2A). Relatively higher transfer efficiency (~90%) or slower attenuation of sinking $CaCO_3$ fluxes (~10%) occur under oligotrophic regions, where POC export from the euphotic zone is lowest. Such biological export-dependent (or remineralization-dependent) transfer/dissolution efficiencies are qualitatively consistent with the observed contrasts between the eutrophic and oligotrophic regions, found for the North Pacific (*15*) and the North Atlantic (Fig. 3 and figs. S5 and S6) (*20*). The sediment trap data thus provide independent support for our best estimates constrained by the $CaCO_3$ burial fluxes and alkalinity distribution.

Further independent support for the tight association between POC remineralization and shallow $CaCO_3$ dissolution comes from the suspended particle concentration data collected using large-volume pumps (*34*–*36*), although a direct comparison is made difficult because we do not explicitly simulate $CaCO_3$ concentrations in our model (see Materials and Methods). The data along the eastern equatorial Pacific (*35*) (chosen based on the best quality control; see Materials and Methods) exhibit a large range of 26 to 88% in the vertical attenuation of $CaCO_3$ concentration within the upper 300 m

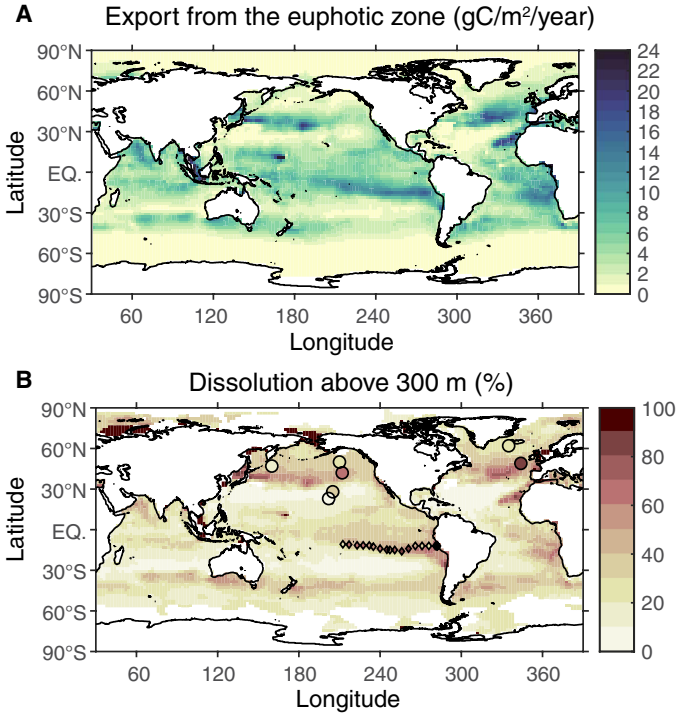

Fig. 1. $CaCO_3$ export from the euphotic zone and dissolution fractions within the upper 300 m. (**A**) The vertical export of $CaCO_3$ from the euphotic zone. The base of the euphotic zone in our model varies from a depth of 73 m in eutrophic regions to 114 m in oligotrophic and highly convective high-latitude regions. (**B**) The fraction at which the $CaCO_3$ exported from the euphotic zone is dissolved until it reaches a depth of 300 m. The shading shows our best estimate. The regions with very low $CaCO_3$ export leading to spurious fractions are masked as white. The filled circles show the sediment trap data–based estimates (see Fig. 3 and figs. S5 and S6 for details). The filled diamonds show the $CaCO_3$ concentration data–based estimates (see Fig. 4 and fig. 7 for details).

(Fig. 4 and fig. S7). The percent attenuation of $CaCO_3$ is positively correlated with the magnitude of POC attenuation with a correlation coefficient of 0.76 ($P < 0.01$ based on a t test). Together, the flux and concentration data support a wide range of $CaCO_3$ dissolution fractions within the upper 300 m of the global ocean (Fig. 1B), which in our model is primarily driven by the POC remineralization rates within the upper twilight zone (see Materials and Methods).

Spatial patterns of $CaCO_3$ dissolution below 300 m and burial fluxes

Below the upper twilight zone , the $CaCO_3$ dissolution patterns are characterized primarily by basin-scale contrasts of the seawater undersaturation states with respect to calcite and aragonite (fig. S4). Distinct dissolution peaks occur in the deep and bottom waters that are undersaturated with respect to aragonite or calcite. The deep ocean dissolution hotspots follow the progressive shoaling of the saturation horizons, the depth above which supersaturated waters lie and below which undersaturated waters lie. When the vertical $CaCO_3$ fluxes are normalized with respect to the vertical fluxes at 300 m, the depth of 30% transfer efficiency (i.e., 70% dissolution) rises from ~4.5 km in the North Atlantic, to ~4 km in the Southern Ocean, and to ~2.5 km in the North Pacific (Fig. 2, B and C). That is, the vertical transfer efficiency of the exported $CaCO_3$ from a depth of 300 m to the seafloor tends to decrease as deep waters become more corrosive (more acidic) from the North Atlantic to the Southern Ocean, and to the North Pacific. The acidity and seawater undersaturation state of deep water appear to be primary drivers of the basin-scale differences in deep ocean $CaCO_3$ dissolution and $CaCO_3$ burial fluxes into sediments.

Spatially varying fractions (e.g., a zonal average ranging from 1 to 52% with an uncertainty range of 1 to 78%) of the surface exported $CaCO_3$ are buried in marine sediments. In general, the burial fractions are higher in less corrosive North Atlantic seafloor and lower in more corrosive North Pacific seafloor (Fig. 2 and fig. S1). Our model captures the observed basin-scale contrasts of $CaCO_3$ burial fluxes arising from the bottom water saturation state, e.g., disproportionately higher burial fluxes in the Atlantic basin than the other basins and near the absence of burial fluxes in the North Pacific (fig. S1). We also find that surface $CaCO_3$ export exerts a large control over the spatial pattern of $CaCO_3$ burial fluxes (*40*), especially for some of the regional burial hotspots in the Atlantic and in the southeastern Pacific. When zonally averaged, the latitudinal bands of elevated burial fluxes coincide with those of higher $CaCO_3$ export from the euphotic zone except for the North Pacific (Fig. 2). More efficient upper water dissolution (i.e., less transfer efficiency) of surface exported $CaCO_3$ under eutrophic surface, relative to oligotrophic surface, tends to dampen the meridional variability of the $CaCO_3$ fluxes reaching the seafloor (fig. S4). Yet, substantial fractions of the surface exported $CaCO_3$ remain undissolved and are buried under highly productive regions, exhibiting burial peaks (Fig. 2 and fig. S1). This direct connectivity from the sea surface to the seafloor makes the $CaCO_3$ burial fluxes a useful constraint for the estimation of the water column $CaCO_3$ export and dissolution (*38*).

Global budget of $CaCO_3$ export, dissolution, and burial

The spatial patterns of the $CaCO_3$ export and dissolution discussed above are consistent with previously suggested global ocean $CaCO_3$ budgets. Globally, our model estimates that 0.40 Pg C $year^{-1}$ (with an uncertainty of 0.26 to 0.46 Pg C $year^{-1}$) of DIC is transferred from land to the open ocean. The estimate is slightly greater than our prescribed riverine DIC flux of 0.30 Pg C $year^{-1}$ (*27*), yet still falls within the uncertainty range. The global integral of the terrestrial DIC fluxes is partly balanced by the global integral of $CaCO_3$ burial fluxes into marine sediments, where our estimate of 0.20 Pg C $year^{-1}$ agrees with an observation-based estimate (*41*). The globally integrated $CaCO_3$ exported from the euphotic zone is estimated to be 1.40 Pg C $year^{-1}$ with an uncertainty range of 0.77 to 1.94 Pg C $year^{-1}$ (Fig. 5A). Global $CaCO_3$ export has been previously suggested to range from 0.4 to 1.8 Pg C $year^{-1}$ (*8*) based on various methodologies, including satellite data in conjunction with $CaCO_3$ sinking flux estimates (*42*), analysis of seasonal decrease in surface alkalinity (*43*), and global ocean and Earth system models (*44*–*47*). Our estimate falls within the upper bound of existing estimates. However, our estimate is substantially larger than the Earth system model-based estimates of 0.66 Pg C $year^{-1}$ provided by the Climate Model Intercomparison Project (CMIP) phase 5, and 0.4 to 1.2 Pg C $year^{-1}$ provided by the CMIP phase 6 (*6*). The upward revision in this study is likely because our estimate implicitly includes the dissolution effects of not only calcite but also more soluble forms of $CaCO_3$ and allows for dissolution above the saturation horizon. Of the $CaCO_3$ exported from the euphotic zone, 37% (with an

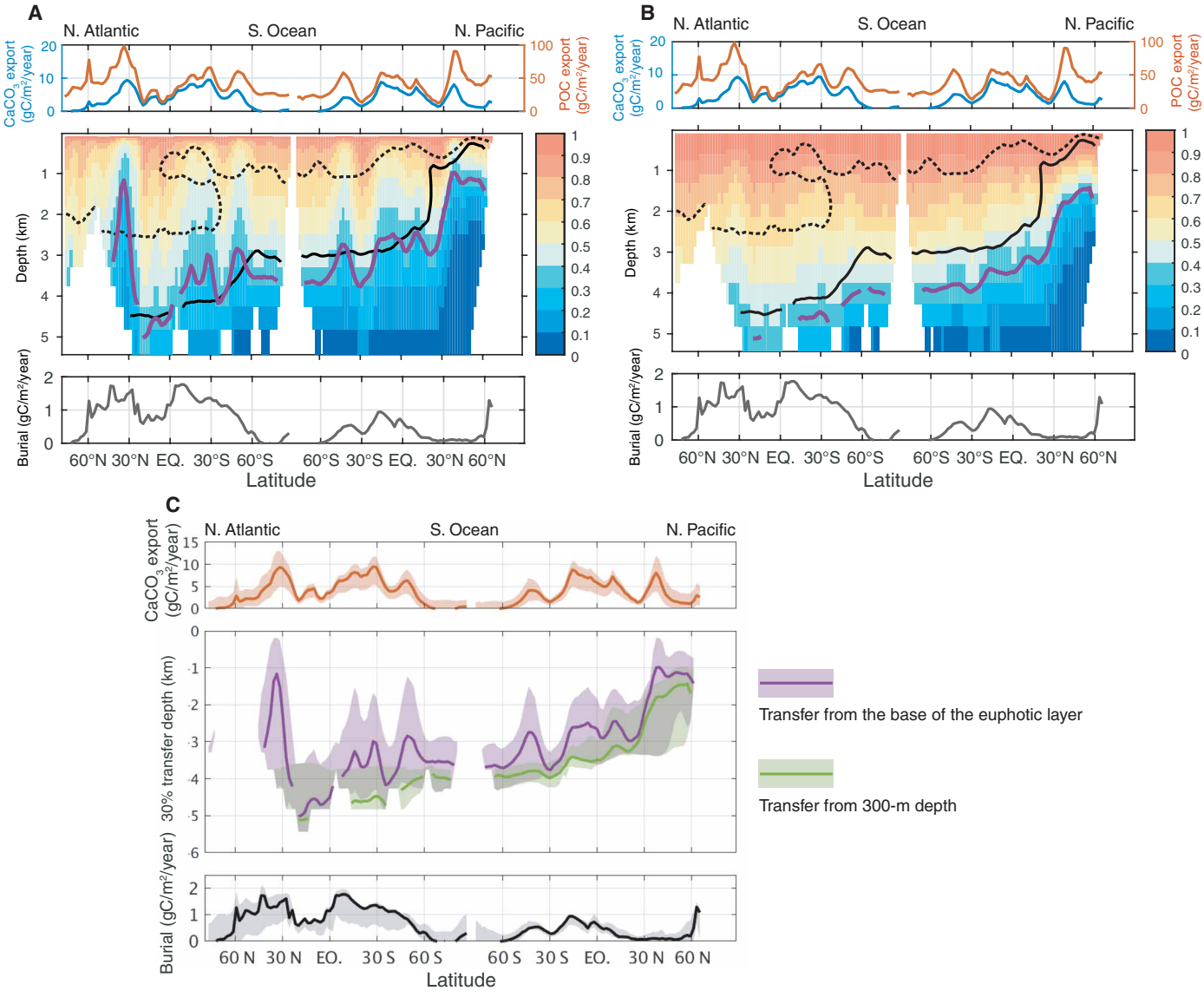

Fig. 2. The zonally averaged vertical transfer efficiencies of sinking $CaCO_3$. The transfer efficiencies (middle) are compared with the zonally averaged $CaCO_3$ and POC export from the euphotic zone (top) and zonally averaged burial fluxes (bottom). The zonal averages from the North Atlantic to the Southern Ocean, and to the North Pacific are shown. (**A**) The vertical $CaCO_3$ fluxes are normalized with respect to the export from the euphotic zone in each water column. The zonal average of the vertical transfer efficiency is shown as shading. The depth by which 30% of the surface exported $CaCO_3$ is transferred (or 70% dissolves) is marked with purple lines. The solid black line represents the calcite saturation horizon, and the dotted black line represents the aragonite saturation horizon. (**B**) Same as (A), except that the vertical $CaCO_3$ fluxes are normalized with respect to the export from a depth of 300 m. (**C**) Uncertainties of the $CaCO_3$ export, the 30% transfer depths, and the burial fluxes are added as shade to the best estimates (respective solid lines).

uncertainty of 5 to 52%) dissolves in the twilight zone shallower than 300 m, where sinking aggregates fluxes rapidly attenuate due to heterotrophic respiration (*20*, *33*). Because of the intensive dissolution in shallow waters, only 0.88 Pg C $year^{-1}$ (with an uncertainty of 0.71 to 0.99 Pg C $year^{-1}$) is exported to depths >300 m, which approximates a recent alkalinity-based estimate of 0.91 ± 0.14 Pg C $year^{-1}$ (*16*) and an inverse model–based estimate of 1.0 Pg C $year^{-1}$ (Fig. 5A) (*19*). At a depth of 2000 m, $CaCO_3$ export is further reduced at 0.43 Pg C $year^{-1}$ (with an uncertainty of 0.41 to 0.50 Pg C $year^{-1}$), which is close to a reported value of 0.6 Pg C $year^{-1}$ derived from sediment trap data (*8*).

$CaCO_3$ dissolution effects on the CO_2 buffer capacity by seawater

To gain an insight into potential drivers of $CaCO_3$ dissolution and its implications on the global carbon cycle, we divided the ocean's interior into three domains depending on the saturation states with respect to $CaCO_3$ minerals: the water that is supersaturated with respect to both calcite and aragonite (referred to as "supersat" zone hereinafter); the water that is supersaturated for calcite, but undersaturated for aragonite (referred to as "midsat" zone); and the water that is undersaturated with both calcite and aragonite (referred to as "undersat" zone) (Fig. 6B). We divided the $CaCO_3$ vertical export

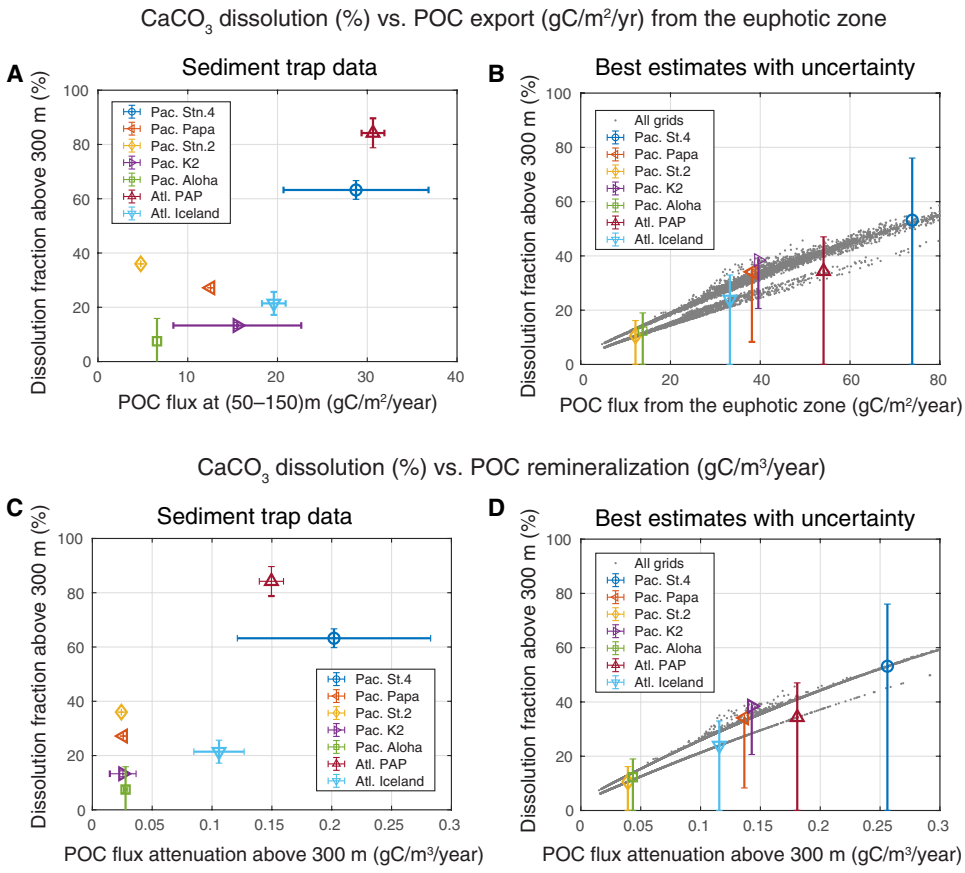

Fig. 3. The relationships between the POC export and remineralization and the $CaCO_3$ dissolution efficiency within the upper twilight zone (≤300 m) estimated using the sediment trap data and the model. (**A**) The relationship between the POC export from the euphotic zone and the upper ocean $CaCO_3$ dissolution fraction estimated using the sediment trap data. The Pacific (Pac.) data are from (*15*, *32*, *33*) with "Stn." representing station (see fig. S5 for vertical fluxes) and the Atlantic (Atl.) data are from (*20*) (see fig. S6 for vertical fluxes) with PAP representing Porcupine Abyssal Plain. A data point closest to the sea surface is assumed to represent the base of the euphotic zone, which varies from 50 to 150 m depending on the stations. Data points located between 151 and 300 m are taken or averaged to estimate the dissolution fraction within the top 300 m. (**B**) Estimates based on our model. The *x* axis shows the POC export from the euphotic zone and the *y* axis shows the $CaCO_3$ dissolution fraction from the base of the euphotic zone to a depth of 300 m. The best estimates sampled from the grid cells corresponding to the sediment trap locations are marked as symbols and the uncertainties are shown as error bars. Gray dots show the best estimates from all grid cells except for the regions where the bathymetry is shallower than 300 m. (**C** and **D**) Same as (A) and (B) except that the *x* axes show the POC flux attenuation (i.e., remineralization) from the euphotic zone to a depth of 300 m. Error bars for the observations are based on the reported values, except that for Pac. K2 and Pac. Aloha the differences in the two measurements are regarded as their uncertainties.

and dissolution into the components that occur within the distinct saturation zones (Fig. 5 and fig. S8). We also diagnosed the distribution of the regenerated DIC and alkalinity, exclusively attributed to the dissolution in each zone (Fig. 6), and assessed how the dissolution contributes to the CO_2 buffer capacity (fig. S9) and air-sea CO_2 exchange (see Discussion and Fig. 7). Dissolution in each zone includes the combined effects of $CaCO_3$ dissolution within the water column and sediments. For clarity, the diagnostics and implications are based on the "Ex_all" experiment where the biological cycling of phosphorus and nitrogen does not influence ocean alkalinity distributions while all else are kept equal to our best solution of the optimization (see Materials and Methods).

When the $CaCO_3$ dissolution is integrated over the distinct saturation zones, the largest portion of total $CaCO_3$ dissolution occurs within the supersat water (i.e., 54% dissolution with an uncertainty of 13 to 66%) (Fig. 5B). When the integrated value is normalized with respect to the mass of water in a unit of micromoles per kilogram per year, the supersat dissolution is two times larger than the global average (Fig. 5C), highlighting the importance of biological controls of $CaCO_3$ dissolution. Despite the global and regional significance in total $CaCO_3$ dissolution (Fig. 5 and fig. S8), the alkalinity regenerated from the supersat dissolution (also known as excess alkalinity) is only up to 15 μeq kg^{-1} and mainly confined in the upper ocean (Fig. 6C) that has relatively short residence time in the ocean's interior. The magnitudes of the regenerated alkalinity are comparable with the model observation misfits (fig. S2). This renders a relatively weak constraint over the upper ocean dissolution, explaining the large uncertainty for the estimated shallow $CaCO_3$ dissolution (Figs. 2C; 3, B and D; and 5; and figs. S5 and S6). Because the supersat dissolution mostly occurs in upper waters below highly productive and upwelling-dominated surfaces (Fig. 2 and fig. S4), an important portion of the regenerated alkalinity would be entrained back to the surface and recycled within the upper ocean with quick turnover timescales, leaving only little imprints on subsurface alkalinity locally. Another

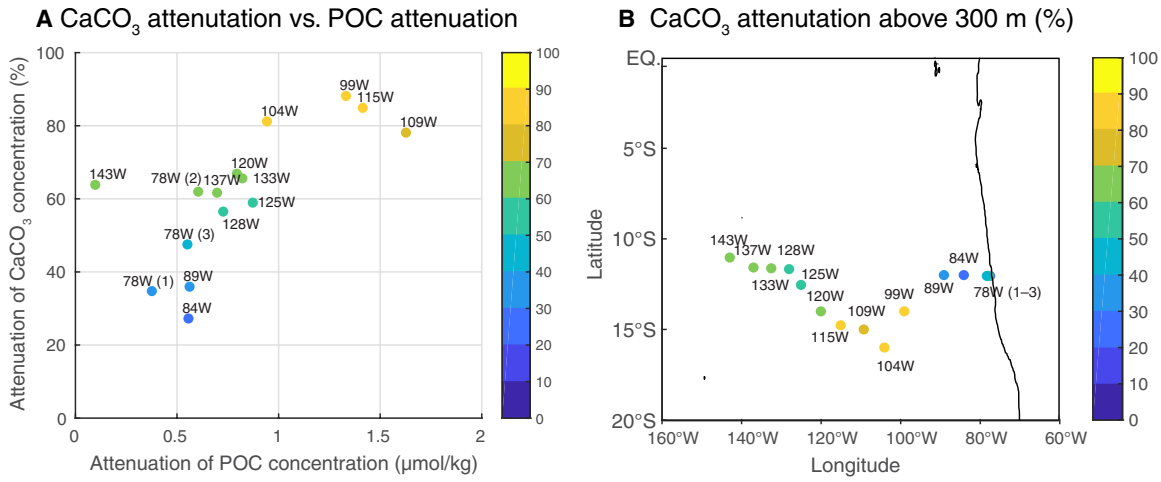

Fig. 4. The relationship between the vertical attenuations of POC and $CaCO_3$ concentrations within the upper twilight zone (≤300 m) estimated using the particle concentration data and the model. (**A**) The relationship between the vertical attenuations of POC and $CaCO_3$ concentrations. The particle concentration data measured using large-volume pumps from (*36*) are used. For each vertical profile, a maximum $CaCO_3$ concentration (within a depth range of 50 to 150 m) and a minimum $CaCO_3$ concentration (within a depth range of 150 to 300 m) are taken to estimate the vertical $CaCO_3$ attenuation fraction. The POC attenuation in the *x* axis is estimated using POC concentrations at the corresponding depths. The $CaCO_3$ attenuation fraction in the *y* axis is also color-coded in each circle. See fig. S7 for the vertical profiles. (**B**) The $CaCO_3$ attenuation fractions are shown at the sampling locations as filled circles. The circles are tagged with the longitude of the sampling locations. The three circles of "78 W (1)," "78 W (2)," and "78 W (3)" fall in a range of 77°30′W to 78°30′W and offshore directed from (1) to (3).

portion of the regenerated alkalinity is transported to the equator where the convergence of global thermocline water results in an accumulation of regenerated alkalinity. Because $CaCO_3$ dissolution increases alkalinity twice as much as an increase of DIC, the $CaCO_3$ dissolution within the supersaturated water has a net effect of up to 6% increases in the CO_2 buffer capacity of the thermocline water (fig. S9).

The effects of $CaCO_3$ dissolution in the midsat and undersat zones, constituting 29% (with an uncertainty of 24 to 58%) and 17% (an uncertainty of 11 to 29%) of total dissolution in the ocean interior (Fig. 5B), respectively, are different from that of the supersat dissolution. Much longer residence times of deep waters allow regenerated DIC and alkalinity to accumulate over longer time periods, elevating alkalinity by up to 50 μeq kg^{-1} for the midsat dissolution and 60 μeq kg^{-1} for undersat dissolution (Fig. 6, D and E). Coupled with the slow deep ocean overturning circulations from the North Atlantic to the Southern Ocean, and to the deep Pacific, dissolutions in the midsat and undersat waters are responsible for the large lateral gradients of alkalinity from relatively young deep Atlantic to old deep Pacific waters. Because of the strong imprints on the large-scale distributions of alkalinity and $CaCO_3$ burial fluxes, the deep ocean $CaCO_3$ dissolution is relatively well constrained in this study, as reflected by relatively smaller uncertainty ranges for the estimated deep ocean dissolution rates (Fig. 5). Figure 6 (D and E) also show that non-negligible portions of the alkalinity regenerated from the deep ocean $CaCO_3$ dissolutions intrude the supersat domain through mixing, as suggested by (*30*). The alkalinity regenerated from the midsat and undersat dissolution contributes to up to 10% of the buffer capacity by mid-depth (1 to 2 km) and deep (3 to 4 km) waters, respectively (fig. S9). The maximum effect of the midsat dissolution is found at mid-depth around ~1500 m in the equatorial Pacific and Indian oceans where a substantial amount of $CaCO_3$ dissolution occurs in the mid-depth aragonite undersaturated water (figs. S4 and S8). On the other hand, the maximum effect of the undersat dissolution is found in the deep North Pacific at depths of ~3500 m where both local dissolution and cumulative effects of remote $CaCO_3$ dissolution contribute to the maximum effects on alkalinity and the CO_2 buffer factor.

DISCUSSION

Our results reveal a previously overlooked sensitivity of upper-ocean $CaCO_3$ dissolution and air-sea CO_2 exchange to organic carbon respiration. We estimated that a global average of 37% (with an uncertainty of 5 to 52%) of the $CaCO_3$ exported from the euphotic zone is dissolved within the upper 300 m, an upper layer of the ocean's twilight zone where most heterotrophic respiration of sinking POC occurs. The fraction at which the surface exported $CaCO_3$ is dissolved (i.e., dissolution efficiency) within the upper 300 m is highly variable in space, which is explicitly tied to the export and remineralization of POC in the ocean's upper twilight zone. This important portion of $CaCO_3$ dissolution has been neglected in previous global-scale assessments, which either focus on the ocean below 300 m or use observed tracer distributions alone as constraints (*16*, *19*, *44*). Our estimated shallow $CaCO_3$ dissolution is only loosely constrained by the observed alkalinity distributions and sedimentary burial fluxes. The weak constraint is reflected by the large error bars for the shallow dissolution (Figs. 2C; 3, B and D; and 5; and figs. S5 and S6) which encompass model solutions with no dependency on POC remineralization (i.e., near zero slopes inferred from Fig. 3, B and D), possibly reconciling this study with previous global-scale estimates.

On the other hand, the data from sediment traps (*15*, *20*, *32*, *33*) and large-volume pumps (*34*–*36*) indicate that the connection between the vertical attenuations in POC and $CaCO_3$ fluxes (or concentrations) within the upper twilight zone might be more robust than our conservative estimate, leaning toward the upper limit of the uncertainty range (i.e., the steepest slopes inferred from

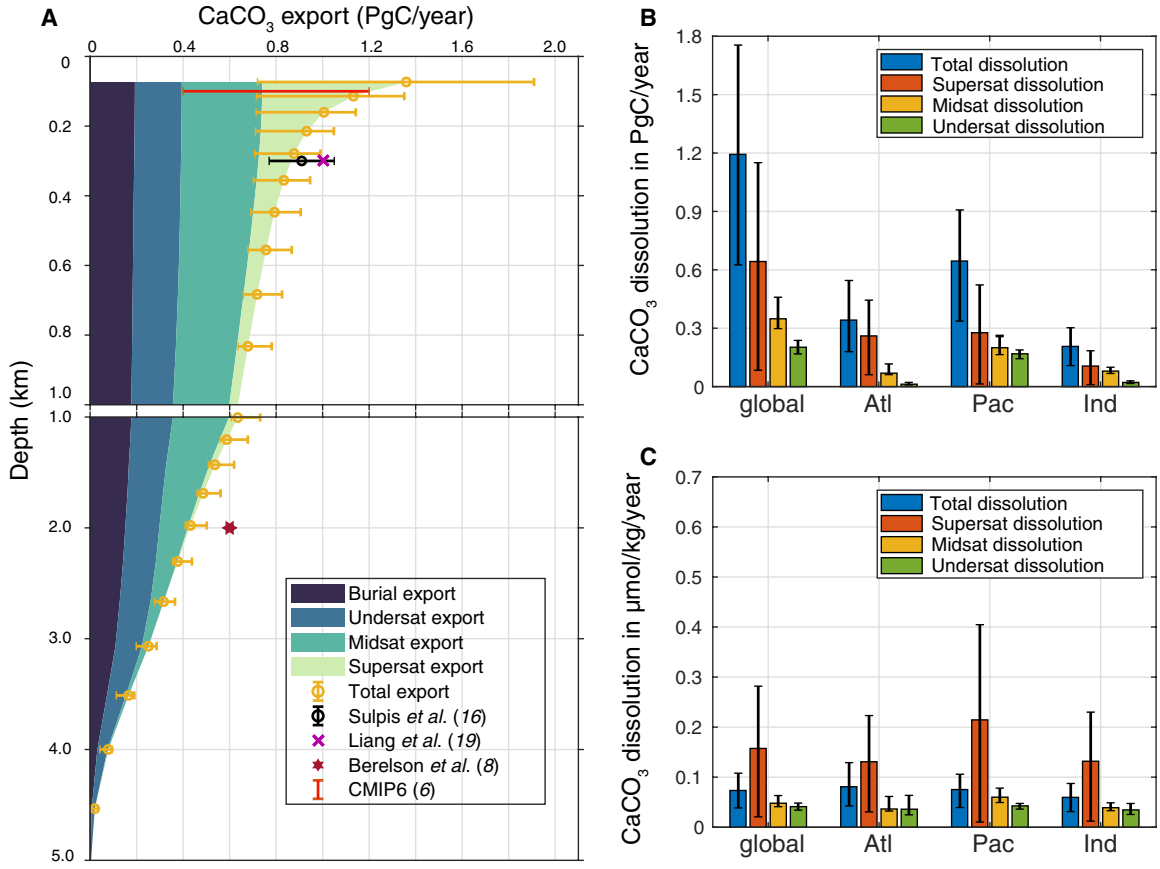

Fig. 5. $CaCO_3$ export and dissolution integrated over the global ocean and basins. (**A**) Globally integrated estimates for the vertical export of $CaCO_3$. The total export from this study is decomposed into the export through three distinct saturation zones and the export that ends up being buried in marine sediments. The three distinct saturation zones include the water supersaturated with respect to calcite and aragonite (supersat), the water supersaturated with calcite, but undersaturated with aragonite (midsat), and the water undersaturated with calcite and aragonite (undersat). The total $CaCO_3$ fluxes at different depth levels from this study (best estimate as yellow circles and the uncertainty as yellow error bars) are compared with the estimates from previous studies. (**B**) $CaCO_3$ dissolution rate is integrated over the three distinct saturation zones. (**C**) Same as (B), except that the integrated estimates are normalized with respect to the mass of the distinct water.

Fig. 3, B and D). The optimal solution in our model is obtained using a linear dependency of the $CaCO_3$ dissolution efficiency on POC remineralization rates with a slope and an intercept determined by the model formulation and optimization (see Materials and Methods). Despite the qualitative agreements, however, there exist large quantitative disparities in the relationships of POC export (and remineralization) versus $CaCO_3$ dissolution efficiency between our model- and observation-based estimates. Part of the differences could be due to the spatial and temporal biases in the flux/concentration measurements and the model uncertainty. The large uncertainties in the observations and in our diagnostic model hamper us from providing a conclusive guideline for the model implementation of the organic carbon respiration control of shallow $CaCO_3$ dissolution. As proven useful in this study, better spatial and temporal coverages of sediment trap and particle concentration data deployed at shallow depths would certainly help better constrain the global ocean $CaCO_3$ cycle and its drivers.

The factors responsible for the biogenic dissolution of sinking $CaCO_3$ in the supersaturated upper water beneath the highly productive surface ocean are still not clearly understood. As constrained in this study, the $CaCO_3$ to POC molar ratio in the exported particles from the euphotic zone tends to be lower in subpolar eutrophic regions compared to low-latitude oligotrophic regions (fig. S3), indicating that sinking aggregates contain more organic carbon per unit $CaCO_3$ under eutrophic regions. The disproportionately larger amount of organic carbon associated with sinking $CaCO_3$ would promote higher rates of respiration-driven dissolution under the eutrophic surface. Moreover, it is also likely that sinking organic carbon under the eutrophic surface is more labile and susceptible to biologically mediated grazing than that under the oligotrophic surface (*48*), the latter which is known to host the microbial community that produces more recalcitrant forms of organic matter (*49*). Disproportionately larger fractions of labile POC or simply larger bulk POC fluxes within the twilight zone below the highly productive surface might attract more heterotrophic respiration, creating corrosive microenvironments for $CaCO_3$ dissolution. The role of heterotrophic respiration in driving $CaCO_3$ dissolution could be effective in slowly sinking particles (*34*, *50*) produced through zooplankton-mediated fragmentation and egestion processes under the eutrophic surface (*51*). The positive correlation between the vertical POC attenuation and the $CaCO_3$ attenuation efficiency shown in Fig. 4 is dominated by small (1 to 53 µm) size classes where the majority of suspended POC and $CaCO_3$ exist (*34*). This implies coccolith calcite and potentially other

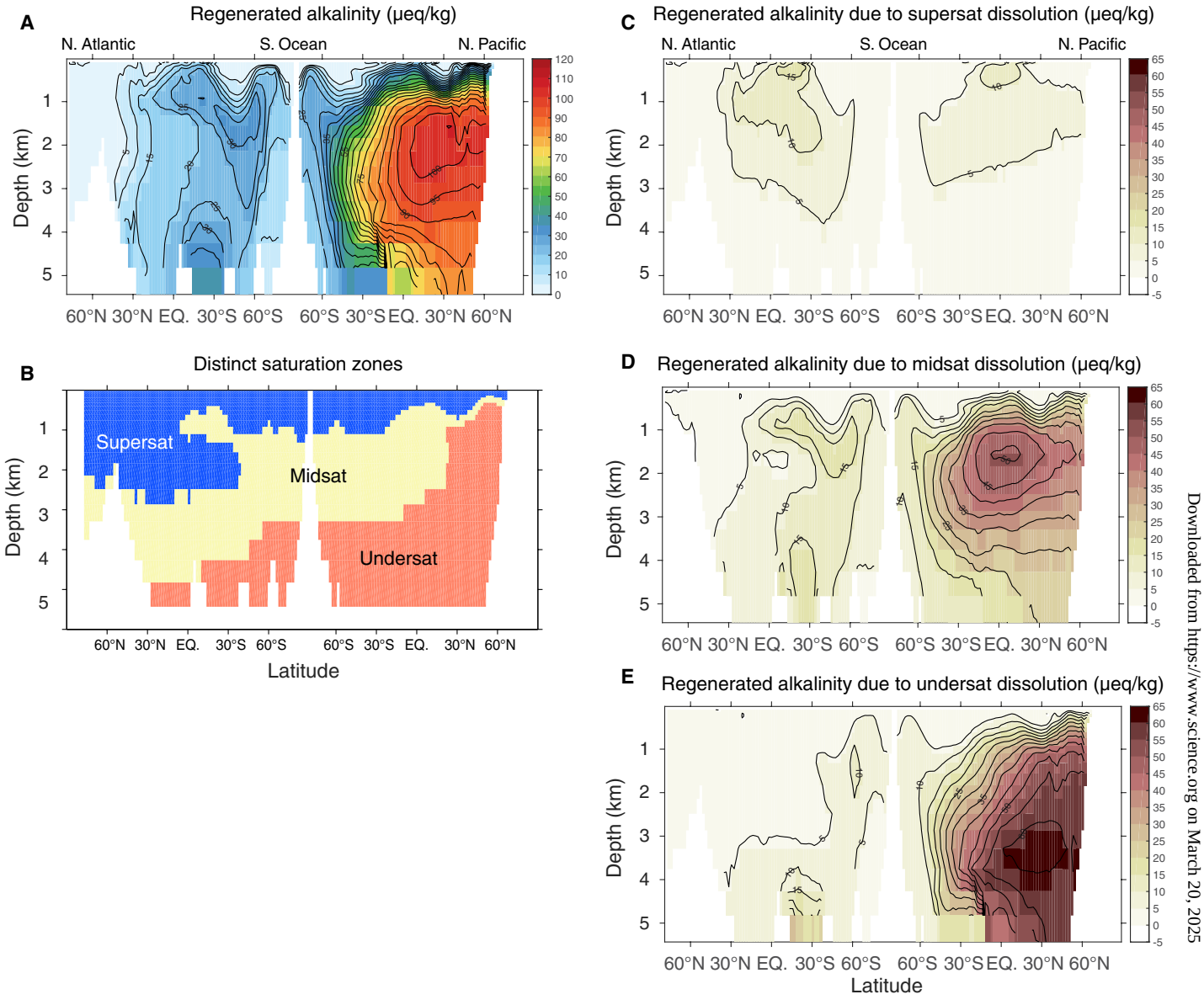

Fig. 6. Zonally averaged regenerated alkalinity from $CaCO_3$ dissolution in distinct saturation zones. This is estimated using the Ex_all experiment where the biological sources and sink of phosphorus and nitrogen are turned off in the best solution of the optimization. (**A**) Total regenerated alkalinity. (**B**) The ocean is grouped into three: the water supersaturated with respect to calcite and aragonite, referred to as supersat; the water supersaturated with respect to calcite, but undersaturated with aragonite, referred to as midsat; and the water undersaturated with calcite and aragonite, referred to as undersat. (**C**) Regenerated alkalinity contribution from the supersat dissolution. (**D**) Regenerated alkalinity contribution from the midsat dissolution. (**E**) Regenerated alkalinity contribution from the undersat dissolution.

small biogenically produced carbonates as the dominant substrate for shallow dissolution, whereas larger organisms such as pteropods and foraminifera sink very quickly due to their large size (*34*). All these potential drivers emphasize the complex interplay between twilight zone biogeochemical processes and upper ocean $CaCO_3$ dissolution.

The dissolution of $CaCO_3$ in shallow waters carries notable implications for the ocean's role in regulating atmospheric CO_2. When the regenerated alkalinity from the supersat dissolution is upwelled to the surface, the excess alkalinity can increase the surface water's CO_2 buffer capacity regionally by up to 5% (Fig. 7B). This implies a reduction of natural CO_2 efflux through the low-latitude upwelling regions (Fig. 7C)—the largest areas of natural CO_2 outgassing in the contemporary climate (*52*). If the supersat dissolution did not occur, then the CO_2 outgassing across the global ocean's 30°S to 30°N band would increase by 20% (a net efflux of 1.0 Pg C $year^{-1}$ with the supersat dissolution versus a net efflux of 1.2 Pg C $year^{-1}$ without the supersat dissolution). This difference in magnitude is comparable to the variability in the equatorial Pacific air-sea CO_2 exchange induced by the El Niño Southern Oscillation, which ranges from 20 to 70%, despite differing drivers (physical versus biological) and timescales (interannual versus a broader spectrum dependent on ecological responses to climate/environmental change).

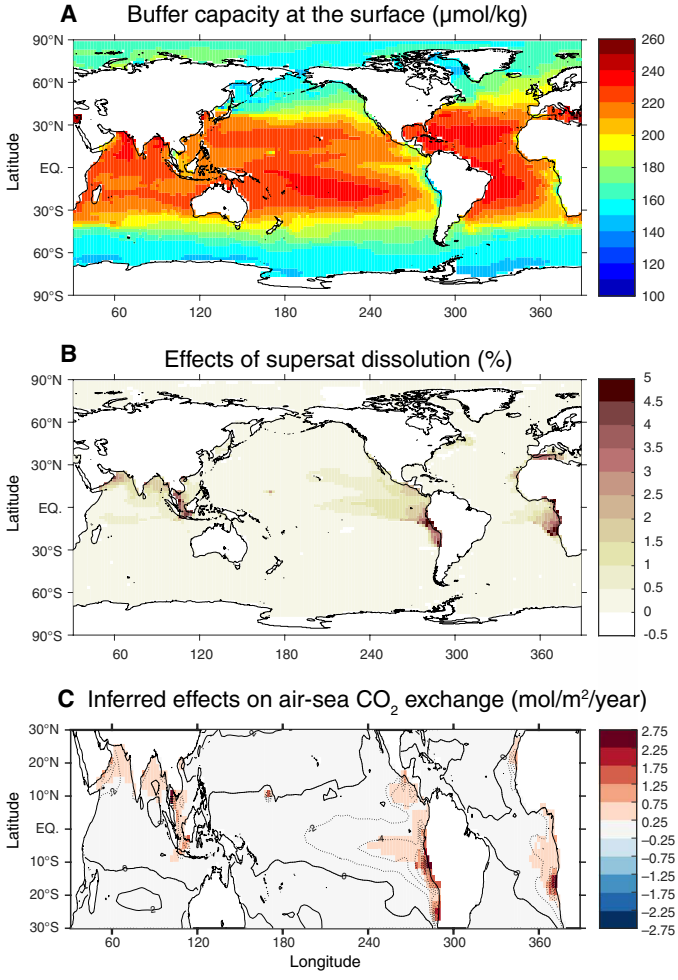

Fig. 7. Implications of the $CaCO_3$ dissolution within the water that is supersaturated with calcite and aragonite on the air-sea CO_2 exchange. (**A**) The buffer capacity (defined as $\partial[DIC]/\partial[CO_2] \times [CO_2]$ where $[CO_2]$ is the concentration of aqueous CO_2 in seawater) at the sea surface estimated using the Ex_all experiment. (**B**) The percentage contribution from the supersat dissolution to the sea surface buffer capacity. (**C**) Shading shows the inferred effects of the supersat dissolution on air-sea CO_2 exchange, i.e., a difference in the air-sea CO_2 exchange between the Ex_all experiment and the case where the effects from the supersat regenerated alkalinity and DIC are removed from the Ex_all experiment. Positive values denote the anomalous fluxes into the ocean (or less efflux into the atmosphere) in mol m^{-2} $year^{-1}$. The contour lines show the preindustrial CO_2 fluxes (in mol m^{-2} $year^{-1}$) simulated from the Ex_all experiment. Positive values (solid lines) denote fluxes into the ocean and negative values (dotted lines) denote fluxes into the atmosphere.

Should the same controls influencing the spatial patterns of $CaCO_3$ dissolution also apply to temporal sensitivity or future climate conditions, a matter requiring validation in future studies, our findings suggest that upper ocean $CaCO_3$ dissolution may not be as responsive to ocean acidification as previously believed. Instead, the response of upper ocean $CaCO_3$ dissolution and the associated change in the ocean's CO_2 buffer capacity would be more influenced by organic carbon export and respiration within the twilight zone. This interplay of $CaCO_3$ dissolution and its subsequent burial into marine sediments introduces a previously unrecognized feedback loop in Earth system models, with far-reaching impacts on marine ecosystems, the global carbon cycle, and climate change.

MATERIALS AND METHODS

Experimental design

We aim to constrain the global ocean patterns of $CaCO_3$ export, dissolution, and burial fluxes into marine sediments and their primary drivers using a numerical model. To this end, we optimized the model parameters representing $CaCO_3$ cycling against multiple observational datasets. To support the biogenic control of $CaCO_3$ dissolution in the upper 300 m, we also analyzed the global compilations of sediment trap data and particle concentration data, both of which are not used to optimize the model and hence provide independent constraints on $CaCO_3$ cycles. Using the constrained numerical model, we performed sensitivity experiments to attribute the simulated tracer distributions and oceanic CO_2 uptake to the $CaCO_3$ dissolution in distinct ocean domains characterized by different saturation states with respect to $CaCO_3$ minerals.

Analyses of $CaCO_3$ and POC flux and concentration data

We used the particle flux data based on sediment traps (*15*, *20*, *32*, *33*) and the particle concentration data based on large-volume pumps (*36*) to estimate the vertical attenuation of the flux and concentrations within the upper 300 m. For the sediment trap data, we assumed that a trap depth closest to the sea surface corresponds to the base of the euphotic zone, which varies from 50 to 150 m depending on the stations. To represent the flux below the euphotic zone, we took or averaged the data points located between 151 and 300 m. A difference between the two data points (one above 151 m and the other below 150 m) is used to estimate the dissolution fraction of $CaCO_3$ flux and the remineralization of POC within the top 300 m. We excluded the sediment trap data where the $CaCO_3$ export from the euphotic zone is very small (<1 g C m^{-2} $year^{-1}$) or the dissolution fractions are negative.

For the particle concentration data (*36*), we subsampled the data within the upper 300 m where both $CaCO_3$ and POC concentrations (in both small and large size classes) have the data quality flag of "0," indicating the best quality control. This criterion screens out most of the data presented in (*34*), giving us only the data collected along the eastern equatorial Pacific (*35*). We combined the small (1 to 53 μm) and large (>53 μm) size classes to represent the $CaCO_3$ and POC concentrations. For each vertical profile, a maximum $CaCO_3$ concentration and a minimum $CaCO_3$ concentration, the latter located below a depth of the maximum value, are taken to estimate the vertical $CaCO_3$ attenuation fraction. The POC attenuation is estimated using POC concentrations at the corresponding depths. This approach helps us link the strongest vertical $CaCO_3$ attenuation with the associated POC attenuation while minimizing potential biases from vertical sampling. We excluded the data where the vertical attenuations of $CaCO_3$ or POC concentrations are negative.

Ocean biogeochemistry model

The model uses a steady-state global ocean circulation inverse model (*23*) that is optimally consistent with observed ocean temperatures, salinity, CFC-11, and deep ocean natural radiocarbon. The horizontal resolution of the model is 2° × 2°, and the vertical grid size increases with depth from 36 m near the surface to 633 m

near the bottom with a total of 24 layers. The model has prognostic tracers of phosphate, alkalinity, DIC, and semi-labile and refractory dissolved organic phosphorus and DOC. The model parameters controlling the export and remineralization of organic carbon and organic phosphorus were previously optimized against the global ocean databases of phosphate, dissolved organic phosphorus, DOC, and DIC (*37*). Built upon the already optimized organic carbon cycle model, in this study, we further elaborated the model formulations and parameterizations representing the export, dissolution, and burial fluxes of $CaCO_3$, and optimized the model parameters against the observed alkalinity and $CaCO_3$ burial fluxes into marine sediments. Below, we briefly review the relevant model formulations representing organic carbon cycling and describe the added formulations for the $CaCO_3$ cycle.

The governing equations for alkalinity (ALK) and DIC are the following

$$\frac{\partial[\mathrm{ALK}]}{\partial t} + U\cdot\nabla[\mathrm{ALK}] - \nabla(K\nabla[\mathrm{ALK}]) = Jb_{\mathrm{ALK}} + Jt_{\mathrm{ALK}} + Jl_{\mathrm{ALK}} + Jv_{\mathrm{ALK}} \quad (1)$$

and

$$\frac{\partial[\mathrm{DIC}]}{\partial t} + U\cdot\nabla[\mathrm{DIC}] - \nabla(K\nabla[\mathrm{DIC}]) = Jb_{\mathrm{DIC}} + Jt_{\mathrm{DIC}} + Jl_{\mathrm{DIC}} + Jv_{\mathrm{DIC}} + Jg_{\mathrm{DIC}} \quad (2)$$

where the three terms on the left-hand side represent the time rates of change in tracer concentrations, and the advective and mixing effects on tracer concentrations. The terms on the right-hand side represent the biological sources and sinks (*Jb*), the terrestrial inputs to the ocean (*Jt*), the sedimentary burial loss (*Jl*), the concentrating and diluting effect due to evaporation and rainfalls (*Jv*), and the air-sea gas exchange (*Jg*). We refer readers to (*37*) for the descriptions of the *Jv* and *Jg* terms, and here, we mainly describe *Jb*, *Jt*, and *Jl* terms.

The net community production of organic carbon is formulated on the basis of the satellite-based estimates for NPP as

$$\mathrm{prodC} = \alpha\frac{(\mathrm{NPP})^{\beta}}{[\mathrm{PO_4}]_{\mathrm{obs}}\cdot Z_{\mathrm{eu}}}[\mathrm{PO_4}]_{\mathrm{mod}} \quad (3)$$

where NPP is the satellite-based estimate for the column-integrated net primary production from (*24*, *25*) in moles of C m^{-2} s^{-1}. Z_{eu} is the thickness of the euphotic layer that varies from 73 m in eutrophic regions to 114 m in oligotrophic and highly convective high-latitude regions. $[PO_4]_{obs}$ and $[PO_4]_{mod}$ are the observed and modeled phosphate concentrations, respectively, the former taken from the World Ocean Atlas (*53*). The ratio of the two can modulate the satellite-based NPP to yield the spatial pattern of net community production (e.g., more production in regions where upwelling increases the ratio of modeled PO_4 to observed PO_4 at the sea surface). Globally uniform values for the two parameters α and β were optimized for the two NPP products separately with the estimates for one NPP presented in table S1 and the estimates for the other NPP presented in (*37*). The export of POC out of the euphotic zone at a horizontal location **r** [termed as $F_{\mathrm{POC}}(z_{\mathrm{eu}}, \mathbf{r})$] is scaled with the net community production with the scaling factor that depends linearly on the euphotic zone temperature. The remaining portion of the net community production is transported as DOC by ocean circulations. The exported POC is assumed to be remineralized instantaneously while sinking. The vertical attenuation profile for downward POC fluxes at **r** follows Martin's power law curve with the exponent linearly scaled with temperatures at 200 m [$T_{200}(\mathbf{r})$] as

$$F_{\mathrm{POC}}(z_n, \mathbf{r}) = F_{\mathrm{POC}}(z_{\mathrm{eu}}, \mathbf{r})\cdot\left(\frac{z_n}{z_{\mathrm{eu}}}\right)^{-b_C(\mathbf{r})} \quad (4)$$

where z_n is the depth of the nth grid cell, which is positive and increases downward. The exponent is formulated as $b_C(\mathbf{r}) = \delta_C \cdot T_{200}(\mathbf{r}) + \gamma_C$ in which δ_C and γ_C were optimized (table S1). The temperature at a depth of 200 m is chosen to represent temperatures (an important environmental factor controlling biological respiration) in the upper twilight zone. b_C is constrained to range from 0.8 in warm subtropical thermocline to 1.0 in cold high-latitude thermocline, possibly reflecting greater lability and grazing of sinking POC in eutrophic waters. Yet, the spatial differences are not statistically significant and depend on the NPP product (*37*).

Similar to POC, $CaCO_3$ is not an explicit tracer in our model, and hence, its biogenic export and dissolution are implicitly represented through downward flux attenuation. The biological sources and sinks for alkalinity are expressed as

$$Jb_{\mathrm{ALK}} = 2Jb_{\mathrm{Ca}} - Jb_{\mathrm{NO3}} - 5.8Jb_{\mathrm{PO4}} \quad (5)$$

where Jb_{Ca} represents the alkalinity sources and sinks due to biogenic $CaCO_3$ cycles, Jb_{NO3} due to biogenic NO_3 cycles, and Jb_{PO4} due to biogenic PO_4 cycles. The factor of two in Jb_{Ca} arises from two moles of alkalinity equivalents consumed and released when a mole of $CaCO_3$ is produced and dissolved, respectively. The factor of −5.8 ($-1 - 2\times 2.4$) in Jb_{PO4} comes from the assumption that a globally uniform stoichiometric ratio of S:P is 2.4 and that two moles of alkalinity equivalents are released and consumed when a mole of SO_4 is produced and remineralized (*29*). Although NO_3 is not a major tracer simulated in our model, its biogenic sources and sinks (Jb_{NO3}) affect alkalinity as shown in Eq. 5. Hence, we linearly scaled the production of organic nitrogen with that of organic carbon using a spatially varying stoichiometric ratio of phytoplankton N:C ratio of rN:C = 125‰ + 30‰ × $[NO_3]_{eu}/(0.32\ \mu\mathrm{mol\ kg^{-1}} + [NO_3]_{eu})$ where $[NO_3]_{eu}$ is the observed NO_3 in the euphotic zone (*54*). We also assumed that the remineralization profile for particulate organic nitrogen and the e-folding timescale for dissolved organic nitrogen remineralization are equal to those of organic carbon. Our Jb_{NO3} term also includes the effects of additional nitrogen sources and sinks due to nitrification and denitrification, taken from (*28*). Hence, the biological source and sink term for NO_3 is Jb_{NO3} = rN:C·Jb_{oc} + nitrification + airborne NO_3 inputs – water column and sediment denitrification (*29*), where Jb_{oc} represents biological sources and sinks of organic carbon. Jb_{DIC} is the sum of Jb_{oc} and Jb_{Ca}.

The Jb_{Ca} term constitutes the export of $CaCO_3$ from the euphotic zone and dissolution throughout the water column and in sediments. The export of $CaCO_3$ from the euphotic zone is proportional to the export of POC with a ratio that depends on the saturation state of surface water (*4*, *5*). We used the following two formulations for the $CaCO_3$ export ratio at the base of the euphotic layer: (i) The export ratio of $CaCO_3$ to POC is linearly scaled with the saturation state of water with respect to calcite as

$$F_{\mathrm{Ca}}(z_{\mathrm{eu}}, \mathbf{r}) = [Al\cdot\Omega^{C}(z_{\mathrm{eu}}, \mathbf{r}) + Bl]\cdot F_{\mathrm{POC}}(z_{\mathrm{eu}}, \mathbf{r}) \quad (6)$$

where $\Omega^{C}(z_{eu}, \mathbf{r})$ is the saturation state with respect to calcite in the euphotic zone, taken from the Global Ocean Data Analysis Project (GLODAP) version 2 (*21*). The globally uniform parameters *Al* and

Bl are optimized in this study (table S1). (ii) The $CaCO_3$ export ratio follows a Michaelis-Menten equation of the saturated state as

$$F_{\mathrm{Ca}}(z_{\mathrm{eu}},\mathbf{r}) = Am \cdot \frac{[\Omega^C(z_{\mathrm{eu}},\mathbf{r})-1]}{Bm+[\Omega^C(z_{\mathrm{eu}},\mathbf{r})-1]} \cdot F_{\mathrm{POC}}(z_{\mathrm{eu}},\mathbf{r}) \quad (7)$$

a formulation similar to that used in (*55*). The maximum value of the export ratio *Am* and a half-saturation constant *Bm* are globally uniform and optimized in this study. The divergence of sinking $CaCO_3$ fluxes (i.e., water column dissolution) is formulated with a first-order rate constant *dissf* that is horizontally and vertically varying as

$$\frac{F_{\mathrm{Ca}}(z_n,\mathbf{r})-F_{\mathrm{Ca}}(z_{n-1},\mathbf{r})}{z_n-z_{n-1}} = -dissf(z_n,\mathbf{r}) \cdot F_{\mathrm{Ca}}(z_{n-1},\mathbf{r}) \quad (8)$$

where $F_{\mathrm{Ca}}(z_n, \mathbf{r})$ is a downward $CaCO_3$ flux exiting the *n*th grid cell, $F_{\mathrm{Ca}}(z_{n-1}, \mathbf{r})$ is equivalent to a $CaCO_3$ flux entering the *n*th grid cell. The rate constant *dissf* is a dissolution constant normalized with respect to the $CaCO_3$ flux from above (in m^{-1}) and can be interpreted as the dissolution rate normalized with respect to the mass of $CaCO_3$ (in a unit of g g^{-1} day^{-1}) divided by the sinking velocity of $CaCO_3$ (in a unit of m day^{-1}). When $dissf(z_n, \mathbf{r})$ is set to zero, none of the $CaCO_3$ dissolves in the grid cell and all $CaCO_3$ passes to the next grid cell. A globally uniform value of *dissf* would yield an exponentially decaying profile of downward $CaCO_3$ fluxes, which was adopted in the simple Ocean Carbon-Cycle Model Intercomparison Project protocol (*56*).

Here, we formulated the dissolution constant *dissf* as

$$dissf(z_n,\mathbf{r}) = \frac{C\cdot\max[0,1-\Omega^C(z_n,\mathbf{r})]^{2.2}+D\cdot\max[0,1-\Omega^A(z_n,\mathbf{r})]^{1.5}+E\cdot R_{\mathrm{POC}}(z_n,\mathbf{r})^G}{vel}+H \quad (9)$$

where $\Omega^C(z_n, \mathbf{r})$ is the saturation state with respect to calcite at a grid cell, $\Omega^A(z_n, \mathbf{r})$ is the saturation state with aragonite. The exponents 2.2 and 1.5 are from field- or lab-based studies (*15*, *57*) and were adopted in a previous modeling study (*19*). The use of 4.7 (*58*) instead of 2.2 as an exponent of $[1-\Omega^C(z_n, \mathbf{r})]$ does not make discernible differences in our conclusion, and the optimal solutions using an exponent of 4.7 are incorporated into our uncertainty range. The previously reported values for *C* and *D* (units of g g^{-1} day^{-1} have large spreads with more than an order of magnitude differences) (*15*, *57*, *58*). Hence, we chose to optimize *C* and *D* (table S1). The sinking velocity of $CaCO_3$ particles, *vel*, is in nature determined by the size and density of sinking particles as well as the viscosity of seawater. Previous studies reported the sinking velocity of $CaCO_3$ ranging from <10 to >150 m day^{-1} (*50*). We assumed that the sinking velocity is a second-order polynomial function of depth as

$$vel = \min\left(vm, v1\cdot {z_n}^2 + v2\cdot z_n + v3\right) \quad (10)$$

where *vm* is a threshold close to zero, needed to avoid zero or negative sinking velocity, and the coefficients *v1*, *v2*, and *v3* are optimized. Our optimization yields the *v1*, *v2*, and *v3* values such that *vel* is converged to a threshold of *vm*, possibly due to dominant controls of the other terms in Eq. 9 on the $CaCO_3$ dissolution constant. Hence, we only report the prescribed *vm* value in table S1. For the respiration control of $CaCO_3$ dissolution, we explored the following two formulations: (iii) R_{poc} is a function of the remineralization rate of POC at a grid cell that is nondimensionalized with an arbitrary constant R_{iii} (in mol m^{-3} s^{-1}) as

$$R_{\mathrm{poc}}(z_n,\mathbf{r}) = \left[-\frac{F_{\mathrm{POC}}(z_n,\mathbf{r})-F_{\mathrm{POC}}(z_{n-1},\mathbf{r})}{z_n-z_{n-1}}\right]\cdot {R_{\mathrm{iii}}}^{-1} \quad (11)$$

(iv) R_{poc} is a function of the remineralization rate of POC normalized with respect to POC flux from above that is nondimensionalized with an arbitrary constant R_{iv} (in m^{-1}) as

$$R_{\mathrm{poc}}(z_n,\mathbf{r}) = \left[-\frac{F_{\mathrm{POC}}(z_n,\mathbf{r})-F_{\mathrm{POC}}(z_{n-1},\mathbf{r})}{z_n-z_{n-1}}\right]\cdot\frac{1}{F_{\mathrm{POC}}(z_{n-1},\mathbf{r})}\cdot {R_{\mathrm{iv}}}^{-1} \quad (12)$$

The scaling factor *E* (a unit of day^{-1}) and the exponent *G* (unitless) are globally uniform parameters to be optimized (table S1). The formulation (iii) would give a *dissf* pattern that is highly variable vertically and horizontally with higher values in the water where POC remineralization is strong. The formulation (iv), which is equivalent to $b_C(\mathbf{r}).(z_{\mathrm{eu}}/z_n)\ .{R_{iv}}^{-1}$, would give a *dissf* pattern that is variable mainly vertically [i.e., due to a relatively smaller horizontal variation in $b_C(\mathbf{r})$ than ${z_n}^{-1}$]. Because all POC fluxes reaching the bottom layer of the ocean model are assumed to be remineralized there [i.e., $F_{\mathrm{POC}}(z_{\mathrm{bottom}}, \mathbf{r}) = 0$], both (iii) and (iv) would give two peaks vertically, the largest peak below the euphotic zone and a secondary peak at the bottom grid cell, the latter depending on bathymetry. The last term in Eq. 9, *H* (a unit of m^{-1}), is included to dampen the horizontal heterogeneity produced by the other terms in Eq. 9 if necessary.

The $CaCO_3$ flux exiting the bottom layer of the ocean model is partitioned into two: A fraction is added to the bottom grid cell representing dissolution in sediments and a remaining fraction is permanently removed from the water column. This removal rate becomes burial fluxes (B_{Ca}) in Jl_{ALK} and Jl_{DIC} in Eqs. 1 and 2 with a 2:1 ratio. The $CaCO_3$ burial flux at a given location is parameterized as

$$B_{\mathrm{Ca}}(z_{\mathrm{bottom}},\mathbf{r}) = F_{\mathrm{Ca}}(z_{\mathrm{bottom}},\mathbf{r})\cdot buryfrac(\mathbf{r}) \quad (13)$$

where $F_{\mathrm{Ca}}(z_{\mathrm{bottom}}, \mathbf{r})$ is the $CaCO_3$ flux exiting the bottom layer of the ocean. The fraction of burial [*buryfrac* (**r**)] is assumed to be linearly scaled with the global patterns of the saturation state with respect to calcite, dissolved O_2 concentrations [O2 where the observed O_2 (in μmol kg^{-1}) is taken from the World Ocean Atlas (*59*)], and the respiration rate of POC (R_{POC} in Eq. 11) at the bottom grid cells of the ocean as

$$\mathrm{buryfrac}(\mathbf{r}) = I\cdot\max[0,1-\Omega^C(z_{\mathrm{bottom}},\mathbf{r})]^{2.2}+ J\cdot\mathrm{O2}(z_{\mathrm{bottom}},\mathbf{r})+K\cdot R_{\mathrm{POC}}(z_{\mathrm{bottom}},\mathbf{r})+M \quad (14)$$

The globally uniform parameters, *I*, *J*, *K*, and a constant *M* are optimized along with other parameters (table S1). We do not distinguish the dissolved $CaCO_3$ in the water column from that in sediments when discussing the results due to the uncertainty in model bathymetry and our simple representation of sedimentary dissolution.

The terrestrial alkalinity source (Jt_{ALK}) includes riverine and non-riverine inputs, the latter of which is estimated in this study. The terrestrial alkalinity fluxes are set to be equal to the terrestrial DIC fluxes given that terrestrial DIC fluxes are mostly in the form of HCO_3^- (*60*). The riverine DIC fluxes are prescribed on the basis of the GEMS-GLORI database (*27*, *61*) and integrated globally to 0.30 Pg C $year^{-1}$ (*61*). To address the uncertainty in the prescribed riverine DIC inputs, and to include additional sources from coastal sediments and aquifers (*62*), we added a spatially uniform flux of DIC at the sea surface around the global coastlines except Antarctica. Assuming a steady-state condition

for the preindustrial times, the terrestrial alkalinity sources need to be balanced by the alkalinity burial sink from the downward $CaCO_3$ fluxes. For this, the magnitude of the non-riverine alkalinity source is estimated such that the globally integrated terrestrial alkalinity source is precisely balanced by the burial fluxes of alkalinity described above. The terrestrial carbon inputs (Jt_{DIC}) include the inorganic (= Jt_{ALK}) and organic forms, the latter prescribed using (*26*, *63*) with a global integral of 0.31 Pg C year^{-1} [see (*61*) for details of the prescribed riverine and air-bourn inputs of terrestrial carbon].

Optimization experiments

We optimized the model parameters (table S1) simultaneously using FMINSEARCH in MATLAB, which uses the unconstrained Nelder-Mead simplex direct search method (*64*). We did not impose any constraints on the signs or ranges of the model parameters so that they are all freely determined by the optimization algorithm. The cost function to be minimized is set as

$$\mathrm{CF} = \frac{\sum \mathrm{Vol}(z_n,\mathbf{r})\cdot[\mathrm{ALK}(z_n,\mathbf{r})^{\mathrm{mod}} - \mathrm{ALK}(z_n,\mathbf{r})^{\mathrm{obs}}]^2}{\sum \mathrm{Vol}(z_n,\mathbf{r})\cdot[\mathrm{ALK}(z_n,\mathbf{r})^{\mathrm{obs}} - \langle \mathrm{ALK}(z_n,\mathbf{r})^{\mathrm{obs}}\rangle]^2} + \frac{\sum \mathrm{Vol}(z_n,\mathbf{r})\cdot[\mathrm{DIC}(z_n,\mathbf{r})^{\mathrm{mod}} - \mathrm{DIC}(z_n,\mathbf{r})^{\mathrm{obs}}]^2}{\sum \mathrm{Vol}(z_n,\mathbf{r})\cdot[\mathrm{DIC}(z_n,\mathbf{r})^{\mathrm{obs}} - \langle \mathrm{DIC}(z_n,\mathbf{r})^{\mathrm{obs}}\rangle]^2} + \frac{\sum \mathrm{Area}(z_{\mathrm{bottom}},\mathbf{r})\cdot[B_{Ca}(z_{\mathrm{bottom}},\mathbf{r})^{\mathrm{mod}} - B_{\mathrm{Ca}}(z_{\mathrm{bottom}},\mathbf{r})^{\mathrm{obs}}]^2}{\sum \mathrm{Area}(z_{\mathrm{bottom}},\mathbf{r})\cdot[B_{Ca}(z_{\mathrm{bottom}},\mathbf{r})^{\mathrm{obs}} - \langle B_{\mathrm{Ca}}(z_{\mathrm{bottom}},\mathbf{r})^{\mathrm{obs}}\rangle]^2} \quad (15)$$

where $\mathrm{Vol}(z_n, \mathbf{r})$ is a grid-cell volume, $\mathrm{Area}(z_{\mathrm{bottom}}, \mathbf{r})$ is a horizontal area, the angle brackets represent the volume- or area-weighted global averages, and the superscripts mod and obs indicate modeled and observed fields. The alkalinity (ALK) and DIC observations are from the GLODAPv2 dataset (*21*) and the observed $CaCO_3$ burial rates (B_{Ca}) are from (*22*). The global datasets are regridded to match the model grid cells (figs. S1 and S2). The estimated distribution of anthropogenic DIC is added to the simulated preindustrial DIC for comparison with observed DIC (*37*). We assumed that the present-day distribution of ocean alkalinity and $CaCO_3$ cycles remain fixed at the preindustrial values.

We performed two sets of optimization experiments with one set using the NPP estimate of (*24*) and the other set using the NPP estimate of (*25*). For each set, four experiments are performed using either one of the formulations for $F_{Ca}(z_{eu}, \mathbf{r})$ (Eq. 5 or Eq. 6) and $dissf(z_n, r)$ (using Eq. 11 or Eq. 12). Of the total eight experiments, the best estimate is chosen from the optimal solution of the best model configuration that yields the minimum value of the cost function. The configuration using the NPP estimate of (*25*) and Eqs. 5 and 11 turns out to yield the best solution after optimization, although other configurations also yield solutions that fall within the uncertainty range. For the uncertainty estimation, we aggregate all the optimization results that use the NPP estimate of (*25*) and apply the criterion of an averaged 1.0% increase in the unexplained variance of alkalinity, DIC, and $CaCO_3$ burial rates relative to the minimum cost function (i.e., a 1.0%-point increase in the cost function). Thus, the uncertainty in model formulations (which is a dominant source of uncertainty than the use of different NPP products) is partly taken into consideration in our uncertainty estimation.

An optimal formulation for $CaCO_3$ dissolution

Here, we provide a formulation of $CaCO_3$ dissolution (both water column and sediments combined) that is optimal for the multiple datasets used in this study. Note that we do not intend to overinterpret individual terms and parameter values obtained in this study (table S1) because some terms are not independent of each other. Moreover, the formulations are meant to be diagnostic for the present-day climate. Nevertheless, it could be informative to describe the optimal formulations obtained in this study.

With our optimized parameter values (table S1), Eq. 8 becomes

$$\frac{F_{\mathrm{Ca}}(z_n,\mathbf{r}) - F_{\mathrm{Ca}}(z_{n-1},\mathbf{r})}{z_n - z_{n-1}} = -\left\{\frac{0.15\cdot\max[0,1-\Omega^C(z_n,\mathbf{r})]^{2.2} + 0.009\cdot\max[0,1-\Omega^A(z_n,\mathbf{r})]^{1.5} + 0.46\cdot R_{\mathrm{POC}}(z_n,\mathbf{r})}{10}\right\}\cdot F_{\mathrm{Ca}}(z_{n-1},\mathbf{r}) \quad (16)$$

where the optimized constant of $H = 0.0002$ (in m^{-1}) is neglected from Eq. 9 due to its relatively minor contribution. By scaling our optimized values of $C = 0.15$ and $D = 0.009$ to $C = 0.50$ g g^{-1} day^{-1} and $D = 0.028$ g g^{-1} day^{-1}, the values previously used in a global ocean modeling study (*19*) based on (*15*, *57*, *58*), the inferred sinking velocity of $CaCO_3$ particles can be scaled from 10 to approximately 30 m day^{-1}, which falls into a reasonable range reported in (*50*). Note however that the large uncertainty in the thermodynamic rate constants (*15*, *57*, *58*) would be directly propagated into an uncertainty in the inferred $CaCO_3$ sinking velocity in this case.

Equation 16 provides further insight into the relationship between the $CaCO_3$ dissolution efficiency and POC remineralization rates in the upper twilight zone where Ω^C and Ω^A are greater than 1 in the majority of the global ocean. The dissolution fraction within the upper 300 m can be approximated as

$$\frac{F_{\mathrm{Ca}}(z_{eu},\mathbf{r}) - F_{\mathrm{Ca}}(300,\mathbf{r})}{F_{\mathrm{Ca}}(z_{eu},\mathbf{r})} = 0.012\cdot\langle R_{\mathrm{POC}}(z_{eu\sim300},\mathbf{r})\rangle'\cdot(300 - Z_{eu}) \quad (17)$$

where Z_{eu} is either 73 or 114 m in our model, which gives rise to two distinct slopes in Fig. 3 (B and D). $\langle R_{\mathrm{POC}}(z_{eu\sim300}, \mathbf{r})\rangle'$ is the POC remineralization rate averaged from the base of the euphotic zone to a depth of 300 m and now expressed in a unit of g C m^{-3} year^{-1} with a scaled coefficient of 0.012 [with a unit of m^2 year (g C)$^{-1}$]. This implies a 12% increase in $CaCO_3$ dissolution fraction when the exported POC increases by 10 g C m^{-2} year^{-1} or a 12% increase in $CaCO_3$ dissolution fraction when the average POC remineralization rate increases by 0.05 g C m^{-3} year^{-1}, which approximate the slopes of the gray dots shown in Fig. 3 (B and D). The intercepts of gray dots in Fig. 3 (B and D) are equal to $H \bullet (300 - Z_{eu})$.

Although it is not a primary focus in this study, we also briefly describe the optimized fraction at which the $CaCO_3$ flux exiting the bottom grid cells of the ocean is buried (*buryfrac* in Eq. 14). The fraction increases from 50% in the shallow regions of the North Pacific and Indian Oceans to 100% in the majority of the Atlantic Ocean. The resulting $CaCO_3$ dissolution in fig. S4 and the burial flux in fig. S1 result collectively from the optimized model formulations described here.

Diagnosing regenerated DIC and alkalinity due to $CaCO_3$ dissolution

On the basis of the optimal model configuration and parameter values, we diagnosed the distributions of alkalinity and DIC that are

regenerated from $CaCO_3$ dissolution in three distinct saturation zones (the undersat, midsat, and supersat zones) (Fig. 6B). This diagnostic has been useful because alkalinity concentration at a given grid cell is the superposition of preformed and regenerated components, the former defined as the alkalinity transported from the sea surface by ocean circulation and the latter defined as the alkalinity added by $CaCO_3$ dissolution. The regenerated component of alkalinity is again the superposition of the effects of $CaCO_3$ dissolution at different grid cells. For clarity in our analyses and interpretation, we first turned off the Jb_{NO3} and Jb_{PO4} terms in Eq. 5 while keeping the other terms and parameterizations fixed at those for the optimal solution. A steady-state solution from this modified model configuration is named "Ex_all." Then, we performed the following model experiments based on the Ex_all configuration.

In the "Ex_No_undersat" experiment, we turned off the $CaCO_3$ dissolution (i.e., $dissf = 0$ and $buryfrac = 1$) in the undersat zone, while $CaCO_3$ dissolution is allowed to occur in the supersat and midsat zones. In the "Ex_No_under_midsat" experiment, we turned off the $CaCO_3$ dissolution in the undersat and midsat zones, while $CaCO_3$ dissolution is allowed to occur in the supersat zone. In the "Ex_No_diss" experiment, we turned off the $CaCO_3$ dissolution in all of the three saturation zones so that all of the $CaCO_3$ exported from the euphotic zone passed through the water column and was buried in sediments. In each experiment, we obtained steady-state solutions and subtracted the estimated preformed alkalinity from the simulated alkalinity to obtain the regenerated (i.e., excess) alkalinity from $CaCO_3$ dissolution, which is equivalent to two times regenerated DIC, following the approach of (*65*).

The difference in regenerated alkalinity between the Ex_all and Ex_No_undersat experiments is attributed to the regenerated alkalinity originating from the $CaCO_3$ dissolution in the undersat zone. Likewise, the difference in regenerated alkalinity between the Ex_No_undersat and Ex_No_under_midsat experiments is attributed to the regenerated alkalinity originating from the $CaCO_3$ dissolution in the midsat zone. The difference in regenerated alkalinity between the Ex_No_under_midsat and Ex_No_diss experiments, the latter of which is confirmed to be zero everywhere, is attributed to the regenerated alkalinity originating from the $CaCO_3$ dissolution in the supersat zone. The resulting distributions of regenerated alkalinity and DIC are used to assess their effects on seawater buffer capacity of CO_2 as described below.

We estimated the CO_2 buffer capacity in the ocean's interior by applying the simulated DIC and alkalinity obtained from the Ex_all experiment following the method of (*66*). To quantify the effects of the $CaCO_3$ dissolution in the three distinct zones on the buffer capacity, we first removed the respective regenerated components of DIC and alkalinity from the simulated DIC and alkalinity in the Ex_all experiment. The reconstructed DIC and alkalinity were then used to diagnose the CO_2 buffer capacity. The departure from the buffer capacity in the Ex_all experiment is regarded as the contribution from each zone $CaCO_3$ dissolution. This approach was necessary because the preformed components of DIC and alkalinity are unrealistic in the experiments where the water column $CaCO_3$ dissolutions were turned off. The suppression of $CaCO_3$ dissolution in each zone results in increasing the $CaCO_3$ removal rates into marine sediments, which in turn elevates the non-riverine inorganic carbon inputs to the ocean surface and the preformed concentrations in our steady-state model.

We further explored how the supersat $CaCO_3$ dissolution might influence the CO_2 buffer capacity and air-sea CO_2 exchange at the sea surface. For the Ex_all case, we simply used the simulated surface DIC and alkalinity to estimate the CO_2 buffer capacity and air-sea CO_2 fluxes using the preindustrial atmospheric CO_2 concentration of 280 ppm. To reconstruct the surface DIC and alkalinity fields that would be obtained if there were no $CaCO_3$ dissolution in the supersat zone, we first removed the contributions of the regenerated DIC and alkalinity from the DIC and alkalinity simulated in the Ex_all experiment. This reconstructed aphotic zone fields of DIC and alkalinity (without dissolution effects at the supersat zone) were then propagated to the euphotic zone as

$$\mathrm{ALK}(\mathbf{r}_{\mathrm{eu}}) = \sum\nolimits_{\mathbf{r}\mathrm{apho}} \mathrm{ALK}(\mathbf{r}_{\mathrm{apho}}) \cdot \mathrm{f}_{\mathbf{r}\mathrm{apho}}(\mathbf{r}_{\mathrm{eu}}) \tag{18}$$

and

$$\mathrm{DIC}(\mathbf{r}_{\mathrm{eu}}) = \sum\nolimits_{\mathbf{r}\mathrm{apho}} \mathrm{DIC}(\mathbf{r}_{\mathrm{apho}}) \cdot \mathrm{f}_{\mathbf{r}\mathrm{apho}}(\mathbf{r}_{\mathrm{eu}}) \tag{19}$$

where $\mathbf{r}_{\mathrm{eu}}$ is a grid point within the euphotic zone in a three-dimensional space, $\mathbf{r}_{\mathrm{apho}}$ is a grid point within the aphotic zone in a three-dimensional space, $\mathrm{f}_{\mathbf{r}\mathrm{apho}}(\mathbf{r}_{\mathrm{eu}})$ is a propagator based on the steady-state ocean circulation field denoting the volume mixing ratio of water at $\mathbf{r}_{\mathrm{eu}}$ that was transported from $\mathbf{r}_{\mathrm{apho}}$ (*67*). This approach is the same as the one we used to compute the preformed alkalinity except that the direction is reversed from the aphotic zone to the euphotic zone. The estimated euphotic zone DIC and alkalinity were then vertically averaged to compute the CO_2 buffer capacity at the sea surface and air-sea CO_2 exchange in the absence of the $CaCO_3$ dissolution in the supersat zone. The potential contributions from the supersat dissolution to the surface water CO_2 buffer capacity and air-sea CO_2 exchange are then estimated by taking differences from the corresponding estimates based on the Ex_all experiment.

Supplementary Materials

This PDF file includes:

Figs. S1 to S9
Table S1

REFERENCES AND NOTES

1. T. Volk, M. I. Hoffert, *The Carbon Cycle and Atmospheric CO2: Natural Variations Archean to Present* (AGU, 1985), pp. 99–110.
2. R. A. Armstrong, C. Lee, J. I. Hedges, S. Honjo, S. G. Wakeham, A new, mechanistic model for organic carbon fluxes in the ocean based on the quantitative association of POC with ballast minerals. *Deep Sea Res. Part II Top. Stud. Oceanogr.* **49**, 219–236 (2001).
3. M. H. Iversen, H. Ploug, Ballast minerals and the sinking carbon flux in the ocean: Carbon-specific respiration rates and sinking velocity of marine snow aggregates. *Biogeosciences* **7**, 2613–2624 (2010).
4. K. J. Kroeker, R. L. Kordas, R. Crim, I. E. Hendriks, L. Ramajo, G. S. Singh, C. M. Duarte, J. P. Gattuso, Impacts of ocean acidification on marine organisms: Quantifying sensitivities and interaction with warming. *Glob. Chang. Biol.* **19**, 1884–1896 (2013).
5. S. C. Doney, D. S. Busch, S. R. Cooley, K. J. Kroeker, The impacts of ocean acidification on marine ecosystems and reliant human communities. *Annu. Rev. Env. Resour.* **45**, 83–112 (2020).
6. A. Planchat, L. Kwiatkowski, L. Bopp, O. Torres, J. R. Christian, M. Butenschön, T. Lovato, R. Séférian, M. A. Chamberlain, O. Aumont, M. Watanabe, A. Yamamoto, A. Yool, T. Ilyina, H. Tsujino, K. M. Krumhardt, J. Schwinger, J. Tjiputra, J. P. Dunne, C. Stock, The representation of alkalinity and the carbonate pump from CMIP5 to CMIP6 ESMs and implications for the ocean carbon cycle. *EGUsphere* **2022**, 1–76 (2022).

7. W. M. Balch, The ecology, biogeochemistry, and optical properties of coccolithophores. *Ann. Rev. Mar. Sci.* **10**, 71–98 (2018).
8. W. M. Berelson, W. M. Balch, R. Najjar, R. A. Feely, C. Sabine, K. Lee, Relating estimates of CaCO3production, export, and dissolution in the water column to measurements of CaCO3rain into sediment traps and dissolution on the sea floor: A revised global carbonate budget. *Global Biogeochem. Cycles* **21**, (2007).
9. P. Ziveri, W. R. Gray, G. Anglada-Ortiz, C. Manno, M. Grelaud, A. Incarbona, J. W. B. Rae, A. V. Subhas, S. Pallacks, A. White, J. F. Adkins, W. Berelson, Pelagic calcium carbonate production and shallow dissolution in the North Pacific Ocean. *Nat. Commun.* **14**, 805 (2023).
10. E. T. Buitenhuis, M. Vogt, R. Moriarty, N. Bednaršek, S. C. Doney, K. Leblanc, C. le Quéré, Y. W. Luo, C. O'Brien, T. O'Brien, J. Peloquin, R. Schiebel, C. Swan, MAREDAT: Towards a world atlas of MARine Ecosystem DATa. *Earth Syst. Sci. Data* **5**, 227–239 (2013).
11. W. S. Broecker, T. H. Peng, *Tracers in the Sea* (Columbia Univ. Press, 1982).
12. M. N. A. Peterson, Calcite: Rates of dissolution in a vertical profile in the central pacific. *Science* **154**, 1542–1544 (1966).
13. R. S. Keir, The dissolution kinetics of biogenic calcium carbonates in seawater. *Geochim. Cosmochim. Acta* **44**, 241–252 (1980).
14. J. F. Adkins, J. D. Naviaux, A. V. Subhas, S. Dong, W. M. Berelson, The dissolution rate of CaCO3in the ocean. *Ann. Rev. Mar. Sci.* **13**, 57–80 (2021).
15. S. Dong, W. M. Berelson, N. E. Rollins, A. V. Subhas, J. D. Naviaux, A. J. Celestian, X. Liu, N. Turaga, N. J. Kemnitz, R. H. Byrne, J. F. Adkins, Aragonite dissolution kinetics and calcite/aragonite ratios in sinking and suspended particles in the North Pacific. *Earth Planet. Sci. Lett.* **515**, 1–12 (2019).
16. O. Sulpis, E. Jeansson, A. Dinauer, S. K. Lauvset, J. J. Middelburg, Calcium carbonate dissolution patterns in the ocean. *Nat. Geosci.* **14**, 423–428 (2021).
17. R. A. Feely, C. L. Sabine, K. Lee, F. J. Millero, M. F. Lamb, D. Greeley, J. L. Bullister, R. M. Key, T. H. Peng, A. Kozyr, T. Ono, C. S. Wong, In situ calcium carbonate dissolution in the Pacific Ocean. *Global Bigeochem. Cycles* **16**, (2002).
18. A. V. Subhas, S. Dong, J. D. Naviaux, N. E. Rollins, P. Ziveri, W. Gray, J. W. B. Rae, X. Liu, R. H. Byrne, S. Chen, C. Moore, L. Martell-Bonet, Z. Steiner, G. Antler, H. Hu, A. Lunstrum, Y. Hou, N. Kemnitz, J. Stutsman, S. Pallacks, M. Dugenne, P. D. Quay, W. M. Berelson, J. F. Adkins, Shallow calcium carbonate cycling in the North Pacific ocean. *Global Bigeochem. Cycles* **36**, (2022).
19. H. Liang, A. M. Lunstrum, S. Dong, W. M. Berelson, S. G. John, Constraining CaCO3Export and dissolution with an ocean alkalinity inverse model. *Global Bigeochem. Cycles* **37**, e2022GB007535 (2023).
20. C. M. Marsay, R. J. Sanders, S. A. Henson, K. Pabortsava, E. P. Achterberg, R. S. Lampitt, Attenuation of sinking particulate organic carbon flux through the mesopelagic ocean. *Proc. Natl. Acad. Sci. U.S.A.* **112**, 1089–1094 (2015).
21. S. K. Lauvset, R. M. Key, A. Olsen, S. van Heuven, A. Velo, X. Lin, C. Schirnick, A. Kozyr, T. Tanhua, M. Hoppema, S. Jutterström, R. Steinfeldt, E. Jeansson, M. Ishii, F. F. Perez, T. Suzuki, S. Watelet, A new global interior ocean mapped climatology: The 1° × 1° GLODAP version 2. *Earth Syst. Sci. Data* **8**, 325–340 (2016).
22. N. A. O'Mara, J. P. Dunne, Hot spots of carbon and alkalinity cycling in the coastal oceans. *Sci. Rep.* **9**, 4434 (2019).
23. T. DeVries, The oceanic anthropogenic CO2sink: Storage, air-sea fluxes, and transports over the industrial era. *Global Biogeochem. Cycles* **28**, 631–647 (2014).
24. M. J. Behrenfeld, P. G. Falkowski, Photosynthetic rates derived from satellite-based chlorophyll concentration. *Limnol. Oceanogr.* **42**, 1–20 (1997).
25. T. Westberry, M. J. Behrenfeld, D. A. Siegel, E. Boss, Carbon-based primary productivity modeling with vertically resolved photoacclimation. *Global Bigeochem. Cycles* **22**, (2008).
26. E. Mayorga, S. P. Seitzinger, J. A. Harrison, E. Dumont, A. H. W. Beusen, A. F. Bouwman, B. M. Fekete, C. Kroeze, G. van Drecht, Global nutrient export from WaterSheds 2 (NEWS 2): Model development and implementation. *Environ. Modell. Softw.* **25**, 837–853 (2010).
27. M. Meybeck, A. Ragu, GEMS-GLORI world river discharge database (Laboratoire de Géologie Appliquée, Université Pierre et Marie Curie, Paris, France, PANGAEA, 2012).
28. W.-L. Wang, J. K. Moore, A. C. Martiny, F. W. Primeau, Convergent estimates of marine nitrogen fixation. *Nature* **566**, 205–211 (2019).
29. D. A. Wolf-Gladrow, R. E. Zeebe, C. Klaas, A. Körtzinger, A. G. Dickson, Total alkalinity: The explicit conservative expression and its application to biogeochemical processes. *Mar. Chem.* **106**, 287–300 (2007).
30. K. Friis, R. G. Najjar, M. J. Follows, S. Dutkiewicz, Possible overestimation of shallow-depth calcium carbonate dissolution in the ocean. *Global Bigeochem. Cycles* **20**, (2006).
31. C.-T. A. Chen, Shelf- vs. dissolution-generated alkalinity above the chemical lysocline. *Deep Sea Res. Part* 49, 5365–5375 (2002).
32. C. S. Wong, F. A. Whitney, D. W. Crawford , K. Iseki, R. J. Matear, W. K. Johnson, J. S. Page, D. Timothy, Seasonal and interannual variability in particle fluxes of carbon, nitrogen and silicon from time series of sediment traps at Ocean Station P, 1982–1993: Relationship to changes in subarctic primary productivity. *Deep Sea Res. Part* 46, 2735–2760 (1999).
33. K. O. Buesseler, C. H. Lamborg, P. W. Boyd, P. J. Lam, T. W. Trull, R. R. Bidigare, J. K. B. Bishop, K. L. Casciotti, F. Dehairs, M. Elskens, M. Honda, D. M. Karl, D. A. Siegel, M. W. Silver, D. K. Steinberg, J. Valdes, B. van Mooy, S. Wilson, Revisiting carbon flux through the ocean's twilight zone. *Science* **316**, 567–570 (2007).
34. A. V. Subhas, F. J. Pavia, S. Dong, P. J. Lam, Global trends in the distribution of biogenic minerals in the ocean. *J. Geophys. Res. Oceans* **128**, e2022JC019470 (2023).
35. P. J. Lam, J. M. Lee, M. I. Heller, S. Mehic, Y. Xiang, N. R. Bates, Size-fractionated distributions of suspended particle concentration and major phase composition from the U.S. GEOTRACES Eastern Pacific Zonal Transect (GP16). *Mar. Chem.* **201**, 90–107 (2018).
36. F. J. Pavia, S. Dong, P. J. Lam, A. V. Subhas, in *Compiled Global Dataset of PIC/POC and bSi Concentrations Measured by In Situ Pumps on Multiple Research Cruises Conducted From Between 1973 and 2013 (Version 1)*. (Biological and Chemical Oceanography Data Management Office, 2022).
37. E. Y. Kwon, M. Holzer, A. Timmermann, F. Primeau, Estimating three-dimensional carbon-to-phosphorus stoichiometry of exported marine organic matter. *Global Bigeochem. Cycles* **36**, e2021GB007154 (2022).
38. J. Dunne, B. Hales, J. R. Toggweiler, Global calcite cycling constrained by sediment preservation controls. *Global Bigeochem. Cycles* **26**, 10.1029/2010GB003935 (2012).
39. J. L. Sarmiento, J. Dunne, A. Gnanadesikan, R. M. Key, K. Matsumoto, R. Slater, A new estimate of the CaCO3to organic carbon export ratio. *Global Bigeochem. Cycles* **16**, 1107 (2002).
40. D. Archer, A data-driven model of the global calcite lysocline. *Global Bigeochem. Cycles* **10**, 511–526 (1996).
41. J. D. Milliman, Production and accumulation of calcium carbonate in the ocean: Budget of a nonsteady state. *Global Biogeochem. Cycles* **7**, 927–957 (1993).
42. J. P. Dunne, J. L. Sarmiento, A. Gnanadesikan, A synthesis of global particle export from the surface ocean and cycling through the ocean interior and on the seafloor. *Global Bigeochem. Cycles* **21**, 10.1029/2006GB002907 (2007).
43. K. Lee, Global net community production estimated from the annual cycle of surface water total dissolved inorganic carbon. *Limnol. Oceanogr.* **46**, 1287–1297 (2001).
44. G. Battaglia, M. Steinacher, F. Joos, A probabilistic assessment of calcium carbonate export and dissolution in the modern ocean. *Biogeosciences* **13**, 2823–2848 (2016).
45. R. Gangstø, M. Gehlen, B. Schneider, L. Bopp, O. Aumont, F. Joos, Modeling the marine aragonite cycle: Changes under rising carbon dioxide and its role in shallow water CaCO3 dissolution. *Biogeosciences* **5**, 1057–1072 (2008).
46. X. Jin, N. Gruber, J. P. Dunne, J. L. Sarmiento, R. A. Armstrong, Diagnosing the contribution of phytoplankton functional groups to the production and export of particulate organic carbon, $CaCO_3$, and opal from global nutrient and alkalinity distributions. *Global Bigeochem. Cycles* **20**, (2006).
47. A. Ridgwell, J. C. Hargreaves, N. R. Edwards, J. D. Annan, T. M. Lenton, R. Marsh, A. Yool, A. Watson, Marine geochemical data assimilation in an efficient Earth System Model of global biogeochemical cycling. *Biogeosciences* **4**, 87–104 (2007).
48. P. J. Lam, S. C. Doney, J. K. B. Bishop, The dynamic ocean biological pump: Insights from a global compilation of particulate organic carbon, $CaCO_3$, and opal concentration profiles from the mesopelagic. *Global Bigeochem. Cycles* **25**, GB3009 (2011).
49. L. Legendre, R. B. Rivkin, M. G. Weinbauer, L. Guidi, J. Uitz, The microbial carbon pump concept: Potential biogeochemical significance in the globally changing ocean. *Prog. Oceanogr.* **134**, 432–450 (2015).
50. M. Villa-Alfageme, F. de Soto, F. A. C. le Moigne, S. L. C. Giering, R. Sanders, R. García-Tenorio, Observations and modeling of slow-sinking particles in the twilight zone. *Global Biogeochem. Cycles* **28**, 1327–1342 (2014).
51. S. L. C. Giering, R. Sanders, R. S. Lampitt, T. R. Anderson, C. Tamburini, M. Boutrif, M. V. Zubkov, C. M. Marsay, S. A. Henson, K. Saw, K. Cook, D. J. Mayor, Reconciliation of the carbon budget in the ocean's twilight zone. *Nature* **507**, 480–483 (2014).
52. P. Landschützer, N. Gruber, D. C. E. Bakker, U. Schuster, Recent variability of the global ocean carbon sink. *Global Biogeochem. Cycles* **28**, 927–949 (2014).
53. H. E. Garcia, K. W. Weathers, C. R. Paver, I. Smolyar, T. P. Boyer, R. A. Locarnini, M. M. Zweng, A. V. Mishonov, O. K. Baranova, D. Seidov, J. R. Reagan, "World Ocean Atlas 2018, Volume 4: Dissolved inorganic nutrients (phosphate, nitrate and nitrate+nitrite, silicate)" (NOAA Atlas NESDIS, 2018).
54. E. D. Galbraith, A. C. Martiny, A simple nutrient-dependence mechanism for predicting the stoichiometry of marine ecosystems. *Proc. Natl. Acad. Sci. U.S.A.* **112**, 8199–8204 (2015).
55. M. Gehlen, R. Gangstø, B. Schneider, L. Bopp, O. Aumont, C. Ethe, The fate of pelagic CaCO3 production in a high CO2 ocean: A model study. *Biogeosciences* **4**, 505–519 (2007).
56. R. G. Najjar, X. Jin, F. Louanchi, O. Aumont, K. Caldeira, S. C. Doney, J. C. Dutay, M. Follows, N. Gruber, F. Joos, K. Lindsay, E. Maier-Reimer, R. J. Matear, K. Matsumoto, P. Monfray, A. Mouchet, J. C. Orr, G. K. Plattner, J. L. Sarmiento, R. Schlitzer, R. D. Slater, M. F. Weirig, Y. Yamanaka, A. Yool, Impact of circulation on export production, dissolved organic matter, and dissolved oxygen in the ocean: Results from phase ii of the Ocean Carbon-Cycle Model Intercomparison Project (OCMIP-2). *Global Biogeochem.I Cycles* **21**, GB3007 (2007).
57. A. V. Subhas, N. E. Rollins, W. M. Berelson, J. Erez, P. Ziveri, G. Langer, J. F. Adkins, The dissolution behavior of biogenic calcites in seawater and a possible role for magnesium and organic carbon. *Mar. Chem.* **205**, 100–112 (2018).

58. J. D. Naviaux, A. V. Subhas, S. Dong, N. E. Rollins, X. Liu, R. H. Byrne, W. M. Berelson, J. F. Adkins, Calcite dissolution rates in seawater: Lab vs. in-situ measurements and inhibition by organic matter. *Mar. Chem.* **215**, 103684 (2019).
59. H. E. Garcia K. W. Weathers, C. R. Paver, I. Smolyar, T. P. Boyer, R. A. Locarnini, M. M. Zweng, A. V. Mishonov, O. K. Baranova, D. Seidov, J. R. Reagan, "World ocean Atlas 2018, Volume 3: Dissolved oxygen, apparent oxygen utilization, and oxygen saturation" (NOAA Atlas NESDI, 2018).
60. P. A. Raymond, S. K. Hamilton, Anthropogenic influences on riverine fluxes of dissolved inorganic carbon to the oceans. *Limnol. Oceanogr. Lett.* **3**, 143–155 (2018).
61. E. Y. Kwon, T. DeVries, E. D. Galbraith, J. Hwang, G. Kim, A. Timmermann, Stable carbon isotopes suggest large terrestrial carbon inputs to the global ocean. *Global Bigeochem. Cycles* **35**, e2020GB006684 (2021).
62. D. T. Maher, M. Call, I. R. Santos, C. J. Sanders, Beyond burial: Lateral exchange is a significant atmospheric carbon sink in mangrove forests. *Biol. Lett.* **14**, 20180200 (2018).
63. J. F. Lamarque, T. C. Bond, V. Eyring, C. Granier, A. Heil, Z. Klimont, D. Lee, C. Liousse, A. Mieville, B. Owen, M. G. Schultz, D. Shindell, S. J. Smith, E. Stehfest, J. van Aardenne, O. R. Cooper, M. Kainuma, N. Mahowald, J. R. McConnell, V. Naik, K. Riahi, D. P. van Vuuren, Historical (1850–2000) gridded anthropogenic and biomass burning emissions of reactive gases and aerosols: Methodology and application. *Atmos. Chem. Phys.* **10**, 7017–7039 (2010).
64. J. C. Lagarias, J. A. Reeds, M. H. Wright, P. E. Wright, Convergence properties of the nelder-mead simplex method in low dimensions. *SIAM J. Optim.* **9**, 112–147 (1998).
65. E. Y. Kwon, J. L. Sarmiento, J. R. Toggweiler, T. DeVries, The control of atmospheric pCO_2 by ocean ventilation change: The effect of the oceanic storage of biogenic carbon. *GBC* **25**, (2011).
66. M. P. Humphreys, E. R. Lewis, J. D. Sharp, D. Pierrot, PyCO2SYS v1.8: Marine carbonate system calculations in Python. *Geosci. Model Dev.* **15**, 15–43 (2022).
67. F. Primeau, Characterizing transport between the surface mixed layer and the ocean interior with a forward and adjoint global ocean transport model. *J. Phys. Oceanogr.* **35**, 545–564 (2005).

Acknowledgments: We thank A. Timmermann for useful comments and discussions throughout this work and for valuable suggestions for the manuscript. We also thank C. Marsay for sharing the sediment trap data with us. The model simulations were performed in Linux servers that are supported by 2016R1D1A1B04931356 and 2023R1A2C1004025 from the Korean National Research Foundation, the latter funded by G. Kim. We are grateful to the editor and reviewers for helping us improve this work. **Funding:** This work was supported by Institute for Basic Science IBS-R028-D1 (to E.Y.K.), National Research Foundation (NRF) 2016R1D1A1B04931356 (to E.Y.K.), and National Research Foundation (NRF) funded by the Ministry of Science and ICT (2021M316A1089658 for the Carbon Cycle between Oceans, Land, and Atmosphere) (to K.L.). **Author contributions:** Conceptualization: E.Y.K. Methodology: E.Y.K. and J.P.D. Investigation: E.Y.K., J.P.D., and K.L. Visualization: E.Y.K. Writing—original draft: E.Y.K., K.L., and J.P.D. Writing—review and editing: E.Y.K., K.L., and J.P.D. **Competing interests:** The authors declare that they have no competing interests. **Data and materials availability:** The GLODAPv2 data are from https://glodap.info. The $CaCO_3$ burial flux data are from https://agupubs.onlinelibrary.wiley.com/action/downloadSupplement?doi=10.1029%2F2010GB003935&file=gbc1910-sup-0002-ds01.nc. The sediment trap data are from the references cited in this manuscript. The time series data at ALOHA are from https://hahana.soest.hawaii.edu/hot/hot-dogs/interface.html. The suspended particle concentration data are from (*36*). All model results and model code are made available at https://climatedata.ibs.re.kr/data/papers/kwon-et-al-2024-sciadv. All data needed to evaluate the conclusions in the paper are present in the paper and/or the Supplementary Materials.

Submitted 27 September 2023
Accepted 23 February 2024
Published 29 March 2024
10.1126/sciadv.adl0779